

# Rotating Black Holes with Primary Scalar Hair: Shadow Signatures in Beyond Horndeski Gravity

Kourosh Nozari,<sup>1,\*</sup> Milad Hajebrahimi,<sup>1,†</sup> Sara Saghafi,<sup>1,2,‡</sup> G. Mustafa,<sup>3,4,§</sup> and Emmanuel N. Saridakis<sup>5,6,7,¶</sup>

<sup>1</sup>*Department of Theoretical Physics, Faculty of Science, University of Mazandaran,  
P. O. Box 47416-95447, Babolsar, Iran*

<sup>2</sup>*School of Physics, Damghan University, Damghan.  
3671645667, Iran*

<sup>3</sup>*Department of Physics, Zhejiang Normal University, Jinhua 321004, China*

<sup>4</sup>*Research Center of Astrophysics and Cosmology,  
Khazar University, Baku, AZ1096, 41 Mehseti Street, Azerbaijan*

<sup>5</sup>*National Observatory of Athens, Lofos Nymfon, 11852 Athens, Greece*

<sup>6</sup>*Departamento de Matemáticas, Universidad Católica del Norte,  
Avda. Angamos 0610, Casilla 1280 Antofagasta, Chile*

<sup>7</sup>*CAS Key Laboratory for Researches in Galaxies and Cosmology, School of Astronomy and Space Science,  
University of Science and Technology of China, Hefei, Anhui 230026, China*

The Event Horizon Telescope (EHT) image of M87\* provides a direct test of strong-field gravity, measuring an angular shadow diameter  $\theta_d = 42 \pm 3 \text{ } \mu\text{as}$  and a circularity deviation  $\Delta C \leq 0.1$ . Such observations allow quantitative tests of the Kerr paradigm and of possible deviations from the no-hair theorem. In scalar-tensor extensions of gravity, black holes may possess primary scalar hair, introducing an additional independent parameter beyond mass and spin. In this work, we construct rotating black hole solutions with primary scalar hair in beyond Horndeski gravity and analyze their photon regions and shadow formation. We show that the scalar hair parameter  $Q$  induces characteristic modifications of the shadow, and in particular negative  $Q$  enlarges the shadow and reduces its oblateness, while positive  $Q$  shrinks and enhances its distortion. Modeling M87\* within this framework and imposing the EHT bounds on  $\theta_d$  and  $\Delta C$ , we determine the viable  $(a, Q)$  parameter space. We find that current observations do not exclude rotating black holes with primary scalar hair, although the allowed region is significantly restricted for  $Q > 0$ . Finally, the scalar-hair-induced deviations are of order  $\mathcal{O}(\mu\text{as})$ , placing them near the sensitivity threshold of present instruments and within reach of next-generation horizon-scale imaging.

**Keywords:** Astrophysical black holes, Beyond Horndeski Theory, Event Horizon Telescope, Scalar hair

## I. INTRODUCTION

In General Relativity (GR), the no-hair theorem states that stationary black hole solutions are uniquely characterized by a small number of conserved charges, namely mass, angular momentum, and electric charge [1–3]. In realistic astrophysical environments, however, black holes are expected to carry negligible electric charge, since any accumulated charge is efficiently neutralized by surrounding plasma and radiation fields [4, 5]. Consequently, rotating astrophysical black holes are well described by the Kerr metric, which represents the unique asymptotically flat, stationary, vacuum solution of GR under these assumptions.

Despite its remarkable empirical success across a wide range of scales, GR is believed to be incomplete. From a theoretical perspective, higher-derivative extensions of GR arising in renormalization schemes generically introduce ghost instabilities [6]. On the observational side, various cosmological tensions [7] and the evidence for dark matter and dark energy from cosmological surveys [8–11], indicate that either new matter components or modifications of gravitational dynamics may be required. These considerations have motivated extensive investigations of modified theories of gravity.

Gravitational modifications [12] arise by extending the Einstein-Hilbert Lagrangian in various ways, resulting in  $f(R)$  gravity [13],  $f(G)$  gravity [14], Lovelock gravity [15], etc. Nevertheless, one can be based on the torsional formulation and extend it to  $f(T)$  gravity [16], to  $f(T, T_G)$  gravity [17], to  $f(T, B)$  gravity [18], etc. Similarly, one can

\* [knozari@umz.ac.ir](mailto:knozari@umz.ac.ir)

† [m.hajebrahimi@stu.umz.ac.ir](mailto:m.hajebrahimi@stu.umz.ac.ir)

‡ [s.saghafi@umz.ac.ir](mailto:s.saghafi@umz.ac.ir)

§ [gmustafa@zjnu.edu.cn](mailto:gmustafa@zjnu.edu.cn)

¶ [msaridak@noa.gr](mailto:msaridak@noa.gr)

start from the equivalent formulation of gravity in terms of non-metricity, and construct  $f(Q)$  gravity [19],  $f(Q, C)$  gravity [20], etc.

Among alternative frameworks, scalar-tensor theories play an important role, since they represent the most direct and well-controlled extension of GR through the inclusion of an additional scalar degree of freedom. The most general scalar-tensor theory leading to second-order field equations is Horndeski gravity [21–43]. It was later realized, however, that the Horndeski construction does not exhaust all healthy scalar-tensor models. In particular, beyond Horndeski (or GLPV) theories extend the Horndeski framework while preserving the correct number of propagating degrees of freedom through hidden constraints, despite containing higher-order derivatives [44–46]. These theories have attracted considerable interest due to their theoretical consistency and rich phenomenology across cosmological and astrophysical scales [47–57].

A distinctive feature of certain subclasses of beyond Horndeski gravity is the existence of black hole solutions endowed with genuine *primary scalar hair*. Contrary to secondary hair, which is completely determined by the black hole mass and angular momentum, primary scalar hair corresponds to an independent integration constant associated with the scalar field configuration. Recently, Bakopoulos *et al.* constructed explicit static, spherically symmetric black hole solutions with primary scalar hair within shift- and parity-symmetric beyond Horndeski theories [58]. These solutions represent genuine departures from the Kerr geometry while remaining regular and asymptotically flat, thereby providing a well-defined framework for exploring strong-field signatures of scalar-tensor gravity. Related black hole configurations within Horndeski and beyond Horndeski gravity have been studied in various contexts, including black hole thermodynamics, gravitational lensing, and solar-system phenomenology [59–64].

As it is well known, black holes constitute natural laboratories for testing gravity in the strong-field regime. A major observational milestone in this direction has been achieved by the Event Horizon Telescope (EHT) collaboration, which obtained horizon-scale images of the supermassive black holes at the centers of M87 and the Milky Way [65, 66]. Using Very Long Baseline Interferometry, the EHT resolved a central brightness depression interpreted as the black hole shadow, produced by strong gravitational lensing of photons emitted by the surrounding plasma. The shadow of M87\* is broadly consistent with the Kerr prediction, exhibiting an angular diameter of  $42 \pm 3 \mu\text{as}$ , a deviation from circularity  $\Delta C \leq 10\%$ , and an axis ratio  $\lesssim 4/3$  [65, 66]. Nevertheless, the present uncertainties, including limitations in array coverage and in modeling of accretion and emission processes, leave room for moderate deviations from Kerr geometry [67].

Within GR, the shadow of a rotating black hole is determined solely by its mass, spin, and the observer's inclination angle. However, in modified gravity theories additional degrees of freedom can modify null geodesics and consequently alter the size, shape, or displacement of the shadow, even in stationary and asymptotically flat spacetimes [68–70]. Black hole shadows therefore provide a direct probe of the spacetime geometry and, by extension, of the underlying gravitational theory [71–77].

Motivated by these considerations, in the present work we extend the static black hole solutions with primary scalar hair found in [58] to rotating configurations by employing a Newman-Janis-type algorithm, following a procedure commonly adopted in the literature [78, 79]. We analyze the resulting horizon structure and investigate null geodesic motion in the corresponding spacetime, deriving the associated photon regions and shadow observables. Our aim is to determine how the independent scalar hair parameter modifies the shadow morphology relative to the Kerr case, and to assess the extent to which such deviations can be constrained by current EHT observations.

In particular, modeling M87\* as a rotating black hole with primary scalar hair in beyond Horndeski gravity, we impose the observational bounds  $\Delta C \leq 0.1$  and  $39 \mu\text{as} \leq \theta_d \leq 45 \mu\text{as}$  on the parameter space spanned by the spin  $a$  and the scalar hair parameter  $Q$ . While we do not perform a full parameter inference analysis, our goal is to identify the qualitative and quantitative imprints of primary scalar hair on black hole shadows and to examine potential degeneracies between scalar hair and rotation. This approach follows the strategy adopted in the studies of black hole shadows in alternative theories of gravity [80–82].

The manuscript is organized as follows. In Sec. II, we present the rotating black hole solution with primary scalar hair in beyond Horndeski gravity and analyze its horizon structure. In Sec. III, we investigate photon motion and derive the associated photon regions and shadow observables. Section IV discusses the phenomenological implications of the model and analyzes the sensitivity of shadow observables to the underlying parameters, including constraints from EHT observations of M87\*. Finally, in Sec. V, we summarize our results and outline future observational prospects.

## II. BLACK HOLES WITH PRIMARY SCALAR HAIR

In this section we present the gravitational configuration that forms the basis of our analysis. We begin by reviewing the spherically symmetric black hole solution with primary scalar hair constructed in Ref. [58] within a subclass of beyond Horndeski theories [44, 48]. This solution represents a genuine deviation from the Kerr paradigm, since it is

characterized by an independent scalar hair parameter that is not fixed by the mass of the black hole. We then extend this static configuration to a rotating spacetime by employing a revised Newman-Janis algorithm (NJA) [78, 83]. The resulting rotating metric provides the necessary framework for investigating photon motion and shadow formation in the presence of primary scalar hair. This construction allows us to explore how the additional scalar degree of freedom modifies the strong-field geometry relative to the Kerr limit.

### A. Spherically symmetric black hole in beyond Horndeski framework

The action of Beyond Horndeski theories [44, 48] with a scalar field  $\Phi$  possessing the additional shift symmetry  $\Phi \rightarrow \Phi + \text{const.}$  and the parity symmetry  $\Phi \rightarrow -\Phi$  can be read as follows

$$\mathcal{I}[\tilde{g}_{\mu\nu}, \Phi] = \frac{1}{2\kappa} \int d^4x \sqrt{-\tilde{g}} \left\{ G_2(W) + G_4(W) R + \partial_W G_4(W) \left[ (\square\Phi)^2 - (\nabla_\mu\partial_\nu\Phi)(\nabla^\mu\partial^\nu\Phi) \right] \right. \\ \left. + F_4(W) \epsilon^{\mu\nu\rho\sigma} \epsilon^{\alpha\beta\gamma} \partial_\mu\Phi \partial_\alpha\Phi (\nabla_\nu\partial_\beta\Phi)(\nabla_\rho\partial_\gamma\Phi) \right\}, \quad (1)$$

where  $\kappa = 8\pi G_N/c^4$  is the coupling constant (from now on, we implement the natural units  $G_N = \hbar = c = 1$ ),  $\square = \partial^\mu\partial_\mu$  is the d'Alembertian operator,  $\tilde{g}$  is determinant of the background spacetime metric  $\tilde{g}_{\mu\nu}$  with the Ricci scalar  $R$ , and  $G_2$ ,  $G_4$ , and  $F_4$  are three parametrization functions in terms of the scalar field kinetic expression  $W = -(1/2)\partial_\mu\Phi\partial^\mu\Phi$ . Moreover, the additional shift symmetry in the theories causes a time-dependency for the scalar field to the form of

$$\Phi = qt + \Psi(r), \quad (2)$$

where  $\Psi(r)$  can be found in Ref. [58]. In expression (2), the quantity  $q$  plays the role of the primary scalar hair with the dimension of [length] $^{-1}$  to ensure the dimensionless behavior of the scalar field  $\Phi$ .

In order to construct an asymptotically flat black hole endowed with primary scalar hair within shift-symmetric beyond Horndeski gravity, we follow the approach of Ref. [58] and we specify the free functions of the theory accordingly. In particular, we choose

$$G_2 = -\left(\frac{8\eta}{3\lambda^2}\right)W^2, \quad G_4 = 1 - \left(\frac{4\eta}{3}\right)W^2, \quad F_4 = \eta, \quad (3)$$

where  $\lambda$  and  $\eta$  are coupling constants with dimensions of [length] and [length] $^4$ , respectively. Without loss of generality, we take  $\lambda > 0$ , since the theory is invariant under the transformation  $\lambda \rightarrow -\lambda$ , as can be directly verified from (3). On the other hand, the coupling  $\eta$  may take either positive or negative values, leading to qualitatively different behaviors of the resulting solutions.

Solving the field equations corresponding to the action (1) with the above choice of functions, one obtains a static and spherically symmetric black hole solution of the form

$$ds^2 = -f(r) dt^2 + \frac{dr^2}{f(r)} + r^2 d\Omega^2, \quad (4)$$

where  $d\Omega^2 = d\theta^2 + \sin^2\theta d\varphi^2$  is the line element of the unit two-sphere. The metric function  $f(r)$  is given by

$$f(r) = 1 - \frac{2M}{r} + Q \left[ \frac{1}{1 + (r/\lambda)^2} + \frac{\frac{\pi}{2} - \arctan(r/\lambda)}{(r/\lambda)} \right], \quad (5)$$

where we have defined the parameter  $Q \equiv \eta q^4$ . Here,  $M$  corresponds to the Arnowitt-Deser-Misner (ADM) mass of the black hole, while  $q$  is an independent integration constant associated with the scalar field, representing a genuine primary scalar hair.

The corresponding scalar field configuration reads [58]

$$\Phi(t, r) = qt + \Psi(r), \quad [\Psi'(r)]^2 = \frac{q^2}{f^2(r)} \left( 1 - \frac{f(r)}{1 + (r/\lambda)^2} \right), \quad (6)$$

where a prime denotes differentiation with respect to  $r$ . The associated kinetic term of the scalar field is then found to be

$$W = \frac{q^2/2}{1 + (r/\lambda)^2}. \quad (7)$$

As evident from the above expressions, the solution possesses two independent integration constants, namely the mass parameter  $M$  and the scalar charge  $q$ , the latter being unrelated to  $M$  and thus characterizing primary scalar hair. In the limit  $q \rightarrow 0$ , or equivalently  $Q \rightarrow 0$ , the scalar field becomes trivial and the metric function (5) reduces smoothly to that of the Schwarzschild black hole, as expected.

The horizons of the black hole are determined by the real positive roots of  $f(r) = 0$ . Due to the functional form of  $f(r)$ , closed analytic expressions for the horizon radii cannot be obtained. Depending on the values of  $q$ ,  $\eta$ , and  $\lambda$ , the spacetime may exhibit a single event horizon, multiple horizons, or a naked singularity, as discussed in detail in Ref. [58]. In the present work, we restrict ourselves to the physically relevant parameter region for which the solution describes a black hole with a single event horizon  $r_{\text{eh}}$ .

For illustration, in Fig. 1 we display the radial behavior of the metric function  $f(r)$  for representative values of  $M$  and  $Q$ . As we observe, for  $Q < 0$  (corresponding to  $\eta < 0$ ), increasing the magnitude of  $|Q|$  leads to an outward shift of the event horizon, whereas for  $Q > 0$  (i.e.  $\eta > 0$ ) the horizon radius decreases as  $Q$  increases. Furthermore, for  $M = 5\lambda$  we observe a more compact configuration due to the larger mass.

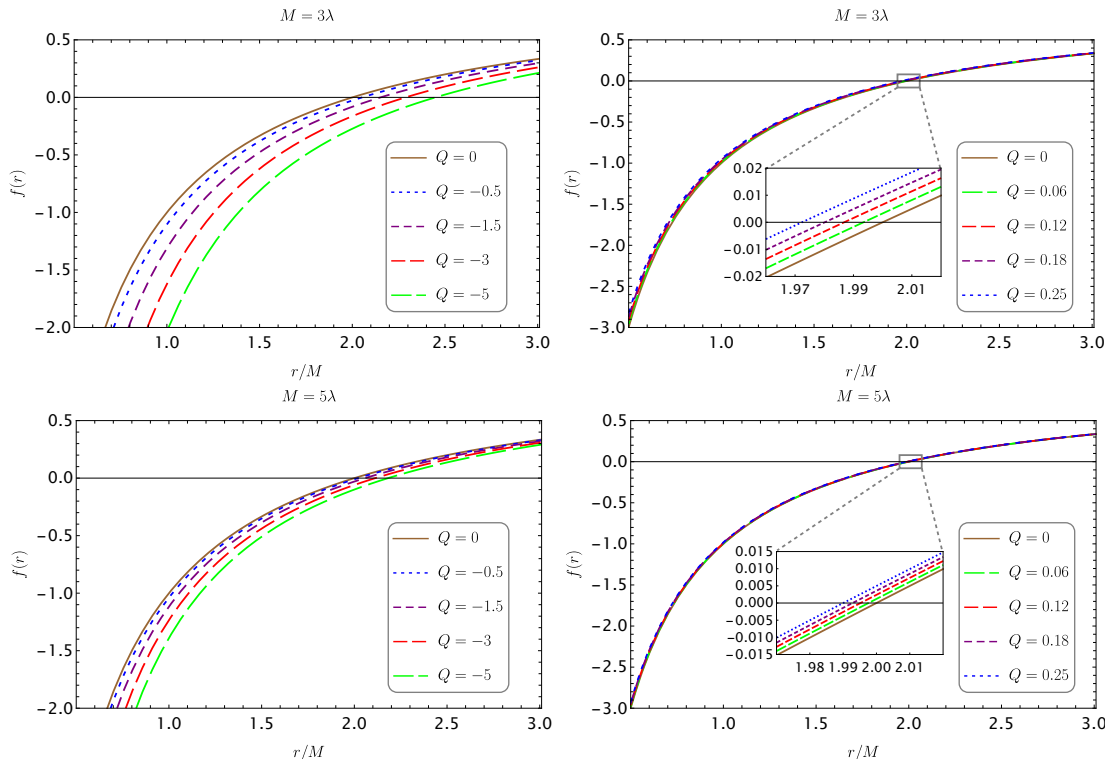


FIG. 1: The radial behavior of the metric function  $f(r)$ . The upper panels correspond to  $M = 3\lambda$  and the lower panels to  $M = 5\lambda$ , while the left panels correspond to  $Q < 0$  and the right panels to  $Q > 0$ .

For completeness, in Table I we summarize the numerical values of the event horizon radius for representative choices of the parameters. As expected, for fixed  $Q$  the horizon radius increases with the mass parameter  $M$ , while for fixed  $M$  the presence of scalar hair modifies the horizon location in a manner controlled by the sign and magnitude of  $Q$ .

TABLE I: The values of single event horizon radii of the asymptotically flat black hole with primary scalar hair in the selected parameter space. The case of  $Q = 0$  represents the Schwarzschild radius with  $r_{\text{Sch}} = 2$ .

horizons	$Q < 0$								$Q > 0$				$\lambda$ values
	$Q = 0$	$Q = -0.5$	$Q = -1.5$	$Q = -3$	$Q = -5$	$Q = 0.06$	$Q = 0.12$	$Q = 0.18$	$Q = 0.25$				
$r_{\text{eh}}$	2	2.053	2.152	2.287	2.448	1.993	1.986	1.980	1.972	$M = 3\lambda$			
$r_{\text{eh}}$	2	2.019	2.057	2.112	2.182	1.997	1.995	1.992	1.990	$M = 5\lambda$			

## B. Rotating black hole configuration with primary scalar hair

The well-known method for converting non-rotating black hole solutions to rotating counterparts is the Newman-Janis algorithm (NJA) [84], which was originally formulated within the framework of the General Theory of Relativity (GR) to form the rotating Kerr black hole from the non-rotating Schwarzschild seed metric. However, the ordinary NJA generally fails to convert the obtained rotating metric from Eddington-Finkelstein coordinates (EFCs) to Boyer-Lindquist coordinates (BLCs) by some real and integrable transformations due to its procedure for complexifying  $r$  coordinate according to our current knowledge [85]. A possible revised version of NJA to solve this failure is proposed in [78, 83] through a non-complexification process, which has attracted much attention. On the other hand, the NJA and its revised version have been applied to many non-rotating black hole solutions within the setup of several modified gravity theories [86–89].

Here, we apply the revised NJA to the line element (4) to obtain the rotating black hole with primary scalar hair in the Beyond Horndeski theories. Consequently, the resulting stationary and axially symmetric version of line element (4) with the metric function (5) in Boyer-Lindquist coordinates can be found as follows (see Appendix A for more details)

$$ds^2 = - \left( 1 - \frac{2\rho(r)}{\Sigma} \right) dt^2 + \frac{\Sigma}{\Delta} dr^2 - \frac{4a\rho(r) \sin^2 \theta}{\Sigma} dt d\varphi + \Sigma d\theta^2 + \sin^2 \theta \left( a^2 + r^2 + a^2 \sin^2 \theta \frac{2\rho(r)}{\Sigma} \right) d\varphi^2, \quad (8)$$

where  $a$  is the spin parameter of the rotating black hole, and also we have defined

$$\Sigma = r^2 + a^2 \cos^2 \theta, \quad \Delta = a^2 + r^2 f(r), \quad 2\rho(r) = a^2 + r^2 - \Delta. \quad (9)$$

From the line element of the rotating black hole with primary scalar hair (8), we can see that in addition to  $M$  and  $a$ , it also depends on  $q$ ,  $\eta$ , and  $\lambda$ . On the other hand, the ordinary Kerr black hole from the rotating black hole with primary scalar hair (8) will recover in the limit  $q \rightarrow 0$  while for  $a \rightarrow 0$ , it will reduce to the asymptotically flat black hole with primary scalar hair (4).

Similar to the Kerr black hole, the line element of the rotating black hole with primary scalar hair (8) has two invariance isometries as time-translational and rotational symmetries corresponding with two Killing vectors  $\chi_{(t)}^\mu = (\frac{\partial}{\partial t})^\mu$  and  $\chi_{(\varphi)}^\mu = (\frac{\partial}{\partial \varphi})^\mu$ , respectively. These Killing vectors admit two conserved quantities in determining the motion of the test particles (omitting the back reaction) around the rotating black hole: the total energy  $E$  and the axial angular momentum  $L_z$ .

The ring singularity of the rotating black hole with primary scalar hair (8) occurs at  $\Sigma = 0$ . On the other hand, the horizons (coordinate singularities) of the rotating black hole occur at  $r$  values satisfying  $\Sigma \neq 0$  and  $g^{\mu\nu} \partial_\mu r \partial_\nu r = g^{rr} = \Delta = 0$  in which  $g_{\mu\nu}$  is the metric tensor of the rotating black hole with primary scalar hair (8). Therefore, the roots of

$$r^2 + a^2 - 2Mr + rQ\lambda \left[ \frac{\pi}{2} + \frac{r\lambda}{\lambda^2 + r^2} - \arctan \left( \frac{r}{\lambda} \right) \right] = 0, \quad (10)$$

are the horizons of the rotating black hole with primary scalar hair (8). However, the analytical expressions of the horizons of the rotating black hole with primary scalar hair cannot be found due to complexity of Eq. (10). Hence, we proceed to find the horizons of the rotating black hole with primary scalar hair, numerically.

In the upper panels of Fig. 2 we depict the behavior of  $\Delta$  versus  $r$  for  $M = 3\lambda$ . As we can see the black hole has generally two horizons: a Cauchy horizon  $r_C$  and an event horizon  $\tilde{r}_{\text{eh}}$ . When  $Q < 0$  (i.e.,  $\eta < 0$ ), the Cauchy horizon is always smaller than the Cauchy horizon of the Kerr black hole and the event horizon is always larger than the event horizon of the Kerr black hole. Additionally, decreasing  $Q$  (i.e., increasing  $q$ ) leads to reduce the Cauchy horizon and amplify the event horizon of the rotating black hole with primary scalar hair. When  $Q > 0$  (i.e.,  $\eta > 0$ ), the Cauchy horizon of the black hole is larger than the Cauchy horizon of the Kerr black hole and its event horizon is smaller than the event horizon of the Kerr black hole. In this situation, for  $Q > 0.06$ , the rotating black hole with primary scalar hair is horizonless and it becomes a naked singularity. Additionally, the lower panes of Fig. 2 illustrate the behavior of  $\Delta$  versus  $r$  for  $M = 5\lambda$ . We observe a similar behavior with the upper panels, except that for  $Q > 0$  (i.e.,  $\eta > 0$ ) the rotating black hole with primary scalar hair is no longer horizonless. Finally, for more transparency, in Table II, we collect the values of the Cauchy horizon  $r_C$  and the event horizon  $\tilde{r}_{\text{eh}}$  of the rotating black hole with primary scalar hair in the parameter space.

Stationary observers located outside the event horizon of a rotating black hole, despite having zero angular momentum relative to an observer at spatial infinity, are compelled to co-rotate with the black hole due to the *frame*

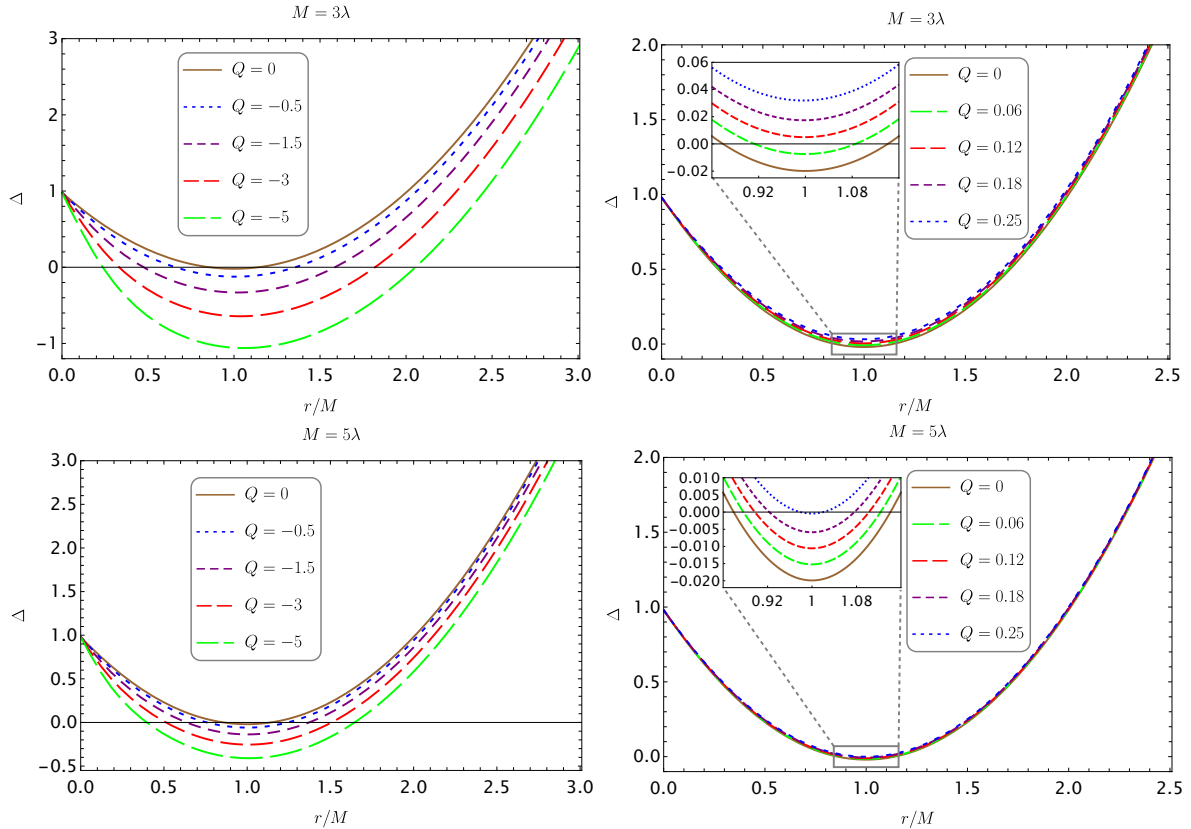


FIG. 2: The behavior of  $\Delta$  versus  $r$ , for various values of  $Q$  and  $a = 0.99$ . The upper panels correspond to  $M = 3\lambda$  and the lower panels to  $M = 5\lambda$ , while the left panels correspond to  $Q < 0$  and the right panels to  $Q > 0$ .

TABLE II: The values of  $r_C$  and  $\tilde{r}_{\text{eh}}$  of the rotating black hole with primary scalar hair in the parameter space. The case of  $Q = 0$  represents horizons of the Kerr black hole. We have set  $a = 0.99$ .

horizons	Kerr	$Q < 0$					$Q > 0$					$\lambda$ values
	$Q = 0$	$Q = -0.5$	$Q = -1.5$	$Q = -3$	$Q = -5$	$Q = 0.06$	$Q = 0.12$	$Q = 0.18$	$Q = 0.25$			
$r_C$	0.858	0.659	0.474	0.331	0.236	0.912						$M = 3\lambda$
$\tilde{r}_{\text{eh}}$	1.141	1.356	1.586	1.819	2.054	1.085						
$r_C$	0.858	0.758	0.635	0.511	0.396	0.876	0.897	0.922	0.979			$M = 5\lambda$
$\tilde{r}_{\text{eh}}$	1.141	1.243	1.371	1.507	1.644	1.123	1.102	1.076	1.019			

dragging effect [90]. Their resulting rotational motion is characterized by the angular velocity  $\omega$ , namely

$$\omega = \frac{d\varphi}{dt} = -\frac{g_{t\varphi}}{g_{\varphi\varphi}} = \frac{2a(a^2 + r^2 - \Delta)}{(a^2 + r^2)^2 - a^2\Delta \sin^2\theta}. \quad (11)$$

In Fig. 3 we present the behavior of the angular velocity. As we can see,  $\omega$  increases monotonically as  $r$  decreases reaching its maximum value at  $r = r_+$ , and is given by

$$\Omega = \omega \Big|_{r=r_{\text{eh}}} = \frac{2a}{a^2 + \tilde{r}_{\text{eh}}^2}, \quad (12)$$

which corresponds to the black hole angular velocity  $\Omega$ .

While stationary observers may exist anywhere outside the event horizon, static observers-whose trajectories are aligned with the timelike Killing vector  $\eta_{(t)}^\mu$ -are restricted to the regions outside the static limit surface (SLS), defined by the condition  $\eta_{(t)}^\mu \eta_{\mu(t)} = g_{tt} = 0$  [90]. The locations of the SLS are obtained from the roots of the equation

$$r^2 + a^2 \cos^2\theta - 2Mr + rQ\lambda \left( \frac{\pi}{2} + \frac{r\lambda}{\lambda^2 + r^2} - \arctan\left(\frac{r}{\lambda}\right) \right) = 0, \quad (13)$$

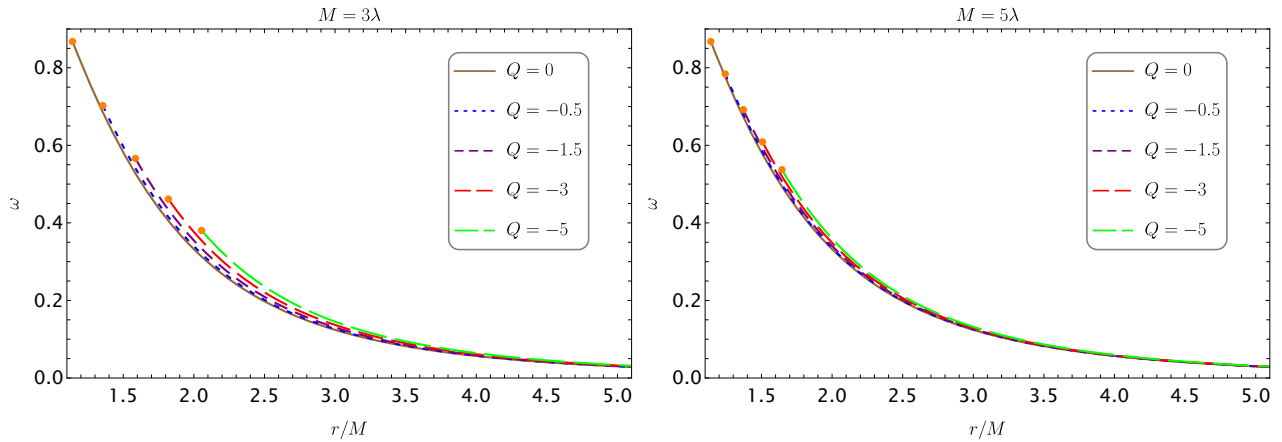


FIG. 3: *Angular velocity  $\omega$  of photons as a function of the dimensionless radial coordinate  $r/M$ , for different values of the scalar hair parameter  $Q$ , in a rotating black hole spacetime with primary scalar hair.*

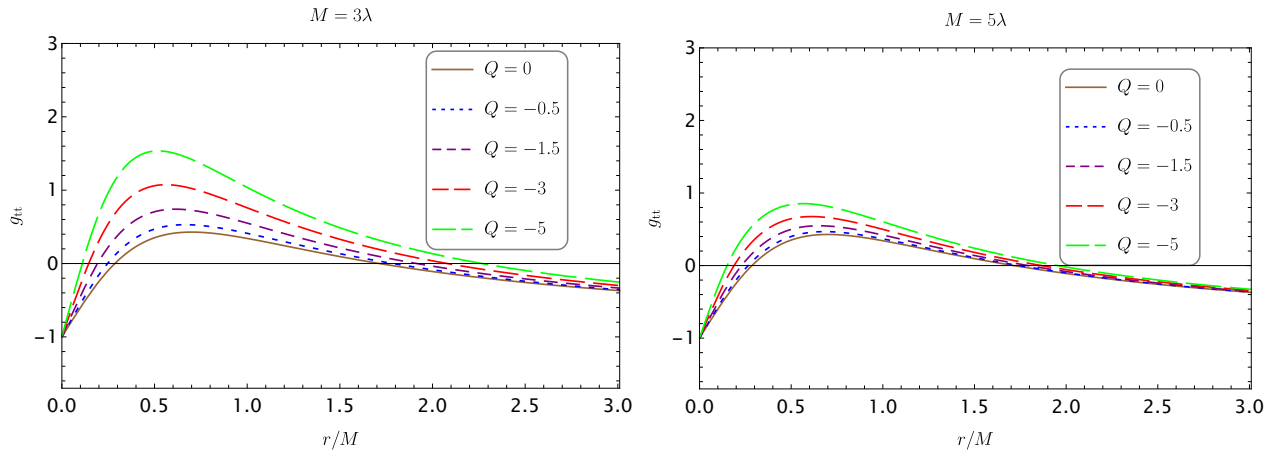


FIG. 4: *The behavior of SLS versus  $r$  for various values of  $Q$  with  $a = 0.99$ .*

which, in addition to the black hole parameters, also depends on the polar angle  $\theta$ , and matches the event horizon only at the poles. We solve Eq. (13) numerically, and the two positive real roots representing the two SLS are plotted in Fig. 4, with  $M = 3\lambda$  and  $M = 5\lambda$  respectively, for different values of  $Q$ . We see that the radius of the outer SLS decreases as  $Q$  increases, and moreover we observe that for fixed values of  $M$  and  $a$  the outer SLS radius of the rotating black hole with primary scalar hair are larger than that of a Kerr black hole.

The region located between the SLS and the event horizon is referred to as the ergoregion. It has been demonstrated that, at least theoretically through the Penrose process [91], energy can be extracted from the black hole's ergosphere, which lies outside the event horizon. In Fig. 5, we show the ergoregion of rotating black hole with primary scalar hair. Interestingly, we find that the shape of the ergosphere becomes increasingly prolate as the scalar hair  $Q$  grows. This indicates that rotating black holes in beyond Horndeski gravity with larger scalar hair values tend to have a more elongated ergosphere, which results in a larger ergospheric area. Furthermore, Fig. 5 shows that there exists some values of the scalar hair for  $M = 3\lambda$ , at which the two surfaces merge into a single one, i.e. for  $Q > 0.06$  the ergoregion disappears entirely. It would be worthwhile to investigate how the scalar hair affects the efficiency of energy extraction, however this study is left for a future project.

### III. PHOTON REGIONS AND SHADOW FORMATION

Having established the rotating black hole geometry with primary scalar hair and analyzed its horizon structure, we now investigate photon motion in this spacetime. The properties of null geodesics determine the photon region and, consequently, the observable shadow of the black hole. Since the shadow boundary corresponds to unstable

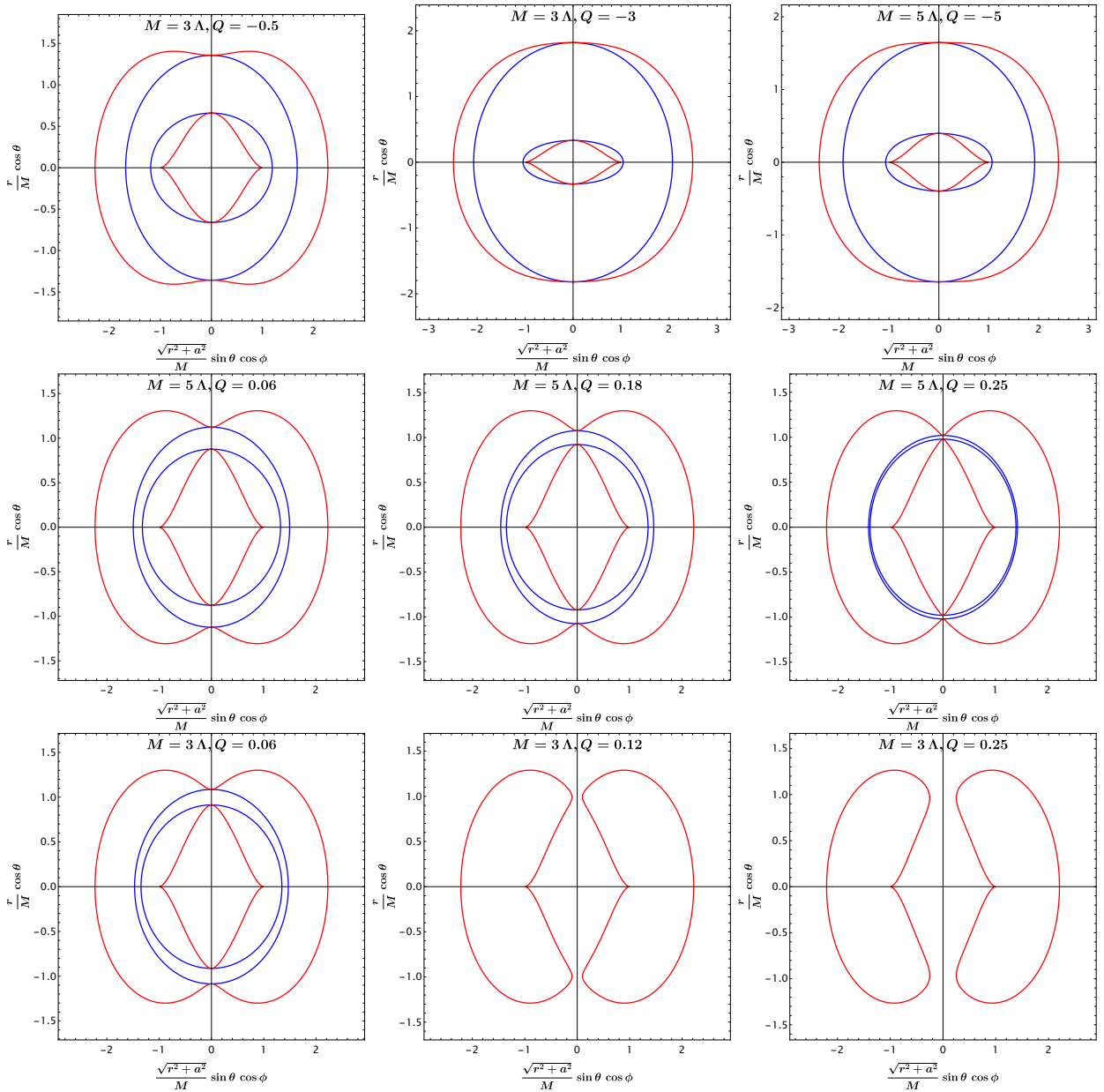


FIG. 5: Cross-sectional profiles of the event horizon (blue), the SLS (red), and the enclosed ergoregion for various values of the parameters  $\lambda$  and  $Q$  with  $a = 0.99$ .

spherical photon orbits, its morphology provides a direct probe of the underlying metric functions. In stationary and axisymmetric spacetimes, the geodesic structure is governed by conserved quantities associated with time-translation and rotational symmetries. In addition, separability of the Hamilton-Jacobi equation allows the introduction of a third constant of motion, leading to a complete characterization of photon trajectories. This structure enables a systematic determination of spherical photon orbits and the associated critical impact parameters.

In the following subsections we first derive the null geodesic equations using the Hamilton-Jacobi formalism and then we construct the photon region and shadow observables. Particular attention is given to how the scalar hair parameter modifies the radial potential and, therefore, the location and stability of photon orbits relative to the Kerr limit.

### A. Null geodesics and photon orbits

We now investigate null geodesics in the spacetime of the rotating black hole with primary scalar hair in beyond Horndeski gravity, described by the line element (8). Since the metric is stationary and axisymmetric, photon motion admits conserved quantities associated with the Killing vectors  $\partial_t$  and  $\partial_\varphi$ . A systematic way to derive the equations of motion is through the Hamilton-Jacobi formalism.

The Hamilton-Jacobi equation reads

$$\frac{\partial \mathcal{S}}{\partial \tau} + \mathcal{H} = 0, \quad (14)$$

where  $\mathcal{S}$  is the Jacobi action, depending on the spacetime coordinates  $x^\mu$  and the affine parameter  $\tau$ . The Hamiltonian for photon motion is

$$\mathcal{H} = \frac{1}{2} g^{\mu\nu} p_\mu p_\nu, \quad (15)$$

with conjugate momentum components

$$p_\mu = \frac{\partial \mathcal{S}}{\partial x^\mu} = g_{\mu\nu} \frac{dx^\nu}{d\tau}. \quad (16)$$

Since the metric (8) does not depend explicitly on  $t$  and  $\varphi$ , the corresponding conjugate momenta are conserved. We therefore define  $p_t = -E$  and  $p_\varphi = L_z$ , where  $E$  and  $L_z$  denote the photon energy and axial angular momentum, respectively.

Assuming separability of the Jacobi action, we write

$$\mathcal{S} = \frac{1}{2} m^2 \tau - Et + L_z \varphi + \mathcal{S}_r(r) + \mathcal{S}_\theta(\theta), \quad (17)$$

where  $m^2 = -p_\mu p^\mu$  is the mass of the test particle. In the present analysis we consider photons, hence  $m = 0$ . The functions  $\mathcal{S}_r(r)$  and  $\mathcal{S}_\theta(\theta)$  are determined by inserting Eq. (17) into the Hamilton-Jacobi equation (14). After straightforward algebraic manipulations, we obtain

$$-\Delta \left( \frac{d\mathcal{S}_r(r)}{dr} \right)^2 + \frac{[(a^2 + r^2)E - aL_z]^2}{\Delta} - (aE - L_z)^2 = \left( \frac{d\mathcal{S}_\theta(\theta)}{d\theta} \right)^2 + \left( \frac{L_z^2}{\sin^2 \theta} - a^2 E^2 \right) \cos^2 \theta. \quad (18)$$

The left-hand side of Eq. (18) depends only on  $r$ , whereas the right-hand side depends solely on  $\theta$ . Both sides must therefore be equal to a constant, which we denote by  $\mathcal{K} = \mathcal{Q} - (aE - L_z)^2$ , where  $\mathcal{Q}$  is the Carter constant [92]. Accordingly, Eq. (18) can be written as

$$\mathcal{K} = -\Delta \left[ \frac{d\mathcal{S}_r(r)}{dr} \right]^2 + \frac{[(a^2 + r^2)E - aL_z]^2}{\Delta} - (aE - L_z)^2, \quad (19)$$

and

$$\mathcal{K} = \left[ \frac{d\mathcal{S}_\theta(\theta)}{d\theta} \right]^2 + \left( \frac{L_z^2}{\sin^2 \theta} - a^2 E^2 \right) \cos^2 \theta. \quad (20)$$

From Eqs. (19) and (20) we obtain

$$\Delta \left[ \frac{d\mathcal{S}_r(r)}{dr} \right]^2 = \frac{[(a^2 + r^2)E - aL_z]^2 - \Delta((aE - L_z)^2 + \mathcal{K})}{\Delta}, \quad (21)$$

and

$$\left( \frac{d\mathcal{S}_\theta(\theta)}{d\theta} \right)^2 = \mathcal{K} - \left( \frac{L_z^2}{\sin^2 \theta} - a^2 E^2 \right) \cos^2 \theta, \quad (22)$$

which determine the radial and angular parts of the motion.

Using Eq. (16), we finally derive the geodesic equations for photons in the rotating black hole spacetime:

$$\Sigma \frac{dt}{d\tau} = \frac{(a^2 + r^2)}{\Delta} [(a^2 + r^2) E - aL_z] - a(aE \sin^2 \theta - L_z), \quad (23)$$

$$\Sigma \frac{dr}{d\tau} = \pm \sqrt{\mathcal{R}(r)}, \quad (24)$$

$$\Sigma \frac{d\theta}{d\tau} = \pm \sqrt{\Theta(\theta)}, \quad (25)$$

and

$$\Sigma \frac{d\varphi}{d\tau} = \frac{a}{\Delta} [(a^2 + r^2) E - aL_z] - \left( aE - \frac{L_z}{\sin^2 \theta} \right), \quad (26)$$

where we have defined

$$\mathcal{R}(r) \equiv [(a^2 + r^2) E - aL_z]^2 - \Delta [(aE - L_z)^2 + \mathcal{K}], \quad \Theta(\theta) \equiv \mathcal{K} - \left( \frac{L_z^2}{\sin^2 \theta} - a^2 E^2 \right) \cos^2 \theta. \quad (27)$$

The allowed region for photon motion is determined by the conditions  $\mathcal{R}(r) \geq 0$  and  $\Theta(\theta) \geq 0$ , which ensure real-valued radial and angular trajectories.

## B. Shadow construction and observables

In order to study the shadow of the rotating black hole with primary scalar hair in beyond Horndeski gravity (8), we first define two impact factors, i.e.,

$$\xi \equiv \frac{L_z}{E}, \quad \zeta \equiv \frac{\mathcal{K}}{E^2}. \quad (28)$$

Now, we can rewrite the functions  $\mathcal{R}(r)$  and  $\Theta(\theta)$  of Eq. (27) in terms of the aforementioned impact factors as

$$\frac{\mathcal{R}(r)}{E^2} = ((a^2 + r^2) - a\xi)^2 - \Delta ((a - \xi)^2 + \zeta), \quad \frac{\Theta(\theta)}{E^2} = \zeta - \left( \frac{\xi^2}{\sin^2 \theta} - a^2 \right) \cos^2 \theta, \quad (29)$$

which again we consider  $\mathcal{R}(r) \geq 0$  and  $\Theta(\theta) \geq 0$  as the allowed region for photon motion.

We aim to study the unstable photon orbits in the spacetime of the rotating black hole with primary scalar hair. According to the values of the critical impact parameters defined above, the photon rays originating from a light source can experience three possible situations: get captured into the rotating black hole; scatter to infinity; construct bound orbits around the black hole.

In studying the shadow of rotating black holes, the spherical (bound) null (photon) orbits living on a sphere with radius  $r = \text{const.} = r_{\text{ph}}$  are important. Thus, these unstable spherical orbits have neither radial velocity  $\dot{r}$  nor radial acceleration  $\ddot{r}$ , where an over dot stands for derivative with respect to  $\tau$ . Therefore, according to Eq. (24), the local extremum  $r_{\text{ph}}$  of the function  $\mathcal{R}(r)$  is the radius of these unstable spherical photon orbits such that

$$\mathcal{R}(r) \Big|_{r=r_{\text{ph}}} = 0, \quad \frac{d\mathcal{R}(r)}{dr} \Big|_{r=r_{\text{ph}}} = 0. \quad (30)$$

Thus, solving simultaneously the set of Eqs. (30) leads to the critical values of the impact parameters for unstable spherical photon orbits as follows

$$\begin{aligned} \xi_{\text{crit}} &= \frac{(a^2 + r^2) \Delta' - 4r\Delta}{a\Delta'}, \\ \zeta_{\text{crit}} &= \frac{r^2 (8\Delta (2a^2 + r\Delta') - r^2 \Delta'^2 - 16\Delta^2)}{a^2 \Delta'^2}. \end{aligned} \quad (31)$$

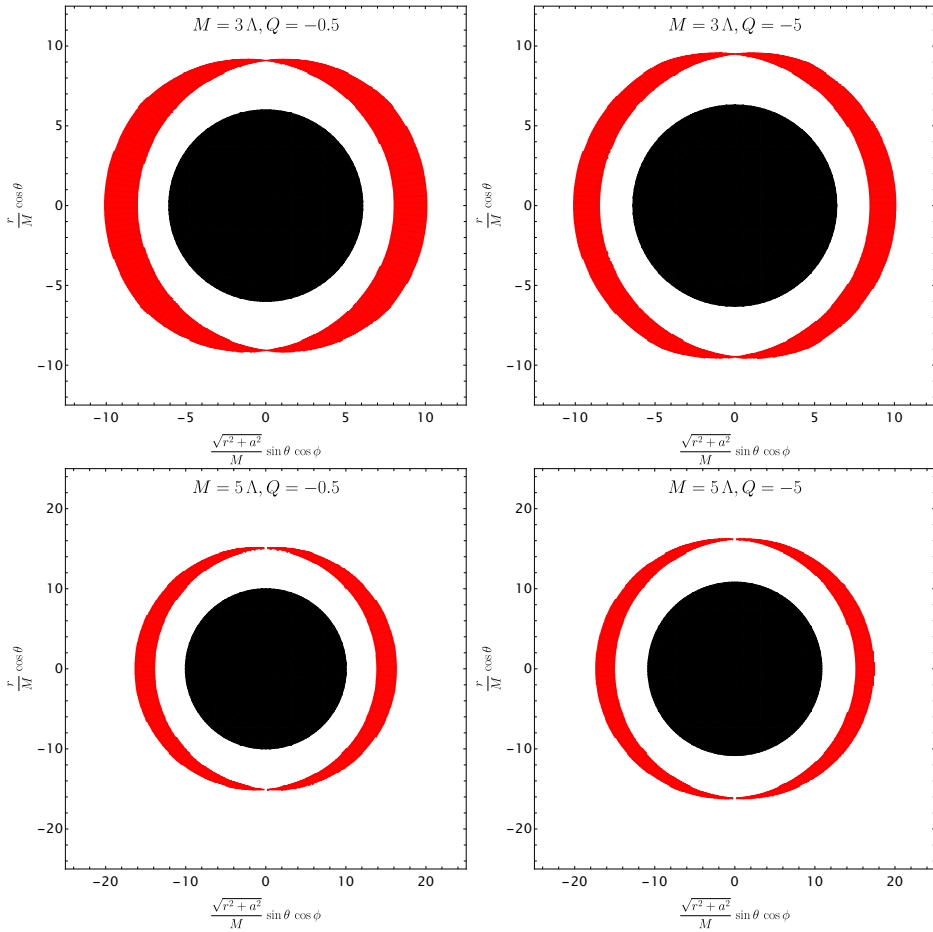


FIG. 6: The configuration of the photon region (shown as the shaded red area) surrounding the rotating black hole with primary scalar hair (depicted as the shaded black disk). We set  $a = 0.99$ .

It is worth noting that the unstable photon orbits are the boundary between capturing and scattering light rays by the rotating black hole, and therefore they are a fruitful tool for characterizing the shape of the shadow of the rotating black hole.

A crucial fact about rotating axisymmetric black hole spacetimes is that around them, there are prograde  $r_{\text{ph}}^-$  and retrograde  $r_{\text{ph}}^+$  unstable photon orbits on the equatorial plane. The prograde/retrograde unstable photon orbits are circulating the rotating black hole in the same/opposite direction as its rotation. Moreover, the prograde unstable photon orbits are smaller than the retrograde ones [93]. Furthermore, the generic spherical (3D and non-planar) photon orbits exist for  $\zeta_{\text{crit}} > 0$  while the circular (planar) photon orbits can occur exclusively on the equatorial plane when  $\zeta_{\text{crit}} = 0$ . The radii  $r_{\text{ph}}^\pm$  of the co-rotating and counter-rotating circular photon orbits correspond to the real positive solutions of  $\zeta_{\text{crit}} = 0$ . These spherical photon orbits form the photon region, which is determined by the equations (27) and (31), subject to the condition  $\Theta(\theta) \geq 0$ . This is given by the inequality:

$$[4r_p\Delta(r_p) - \Delta'(r_p)\Sigma]^2 \leq 16a^2r_p^2\Delta(r_p)\sin^2\theta. \quad (32)$$

As we can see in Fig. 6, the image produced by gravitational lensing of this photon region corresponds to the black hole shadow. Moreover, the photon region, formed by unstable photon orbits, varies with the scalar hair parameter  $Q$  and the mass parameter  $M$ . The different panels show the configurations for various values of  $Q$  (ranging from negative to positive), with  $M = 3\lambda$  and  $M = 5\lambda$ , respectively. These plots highlight how the photon region's shape and size are influenced by changes in  $Q$ , providing insight into how scalar hair affects the black hole's gravitational field and photon dynamics.

The shadow of a black hole is the result of intense gravitational lensing near these compact objects, which distorts the light path and creates a dark zone visible to a distant observer [94–98]. This optical feature appears as a 2D shadow and is influenced by the geometry of the black hole's spacetime. The size and shape of the shadow can be

used to determine key properties of the black hole, such as its mass, spin, and other characteristics. The shadow thus serves as an effective tool for testing modified gravity theories in strong gravitational fields [97, 99], as well as the validity of the no-hair theorem [100]. The photon region surrounding the black hole's event horizon is composed of unstable photon orbits, marking the boundary between those photons that escape to infinity and those that fall into the black hole.

We consider light sources distributed uniformly at infinity, with photons arriving with various impact parameters. These photons either scatter near the black hole's vicinity, or are captured by it. A distant observer is assumed to be at an inclination angle  $\vartheta_o$  relative to the black hole's rotation axis. The coordinates  $(X, Y)$  represent the angular distances of the shadow's boundary from the observer's line of sight in directions perpendicular and parallel to the projected axis of rotation of the black hole onto the celestial plane [101]. By performing a stereographic projection of the black hole's shadow onto the observer's sky, the boundary of the shadow can be described in these celestial coordinates as follows

$$X = \lim_{r_o \rightarrow \infty} \left[ -r_o^2 \sin \vartheta_o \frac{d\varphi}{dr} \Big|_{(r_o, \vartheta_o)} \right], \quad Y = \lim_{r_o \rightarrow \infty} \left[ r_o^2 \frac{d\theta}{dr} \Big|_{(r_o, \vartheta_o)} \right], \quad (33)$$

where  $(r_o, \vartheta_o)$  represent the coordinates of the distant observer who sights the photons along the inclination angle  $\vartheta_o$  coming from the light source deflected by the central rotating black hole, as seen in Fig. 7. The rotating black hole

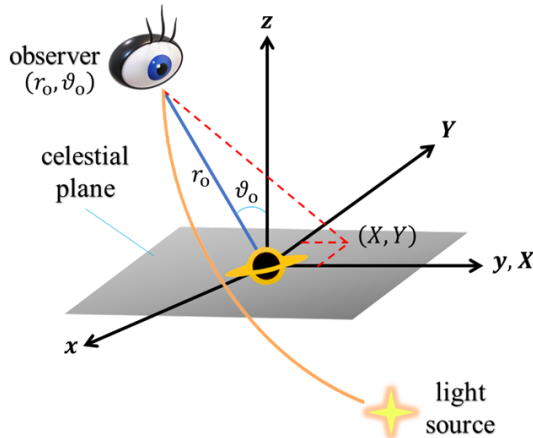


FIG. 7: The diagram of the celestial coordinates on the distant observer's sky, where  $r_o$  represents the spatial separation between the distant observer and the rotating black hole with primary scalar hair, and  $\vartheta_o$  denotes the angular coordinate of the distant observer. The coordinates  $(X, Y)$  indicate the apparent perpendicular distance of the image as observed from the axis of symmetry, and from its projection onto the equatorial plane, respectively.

is a spacetime that is stationary, axisymmetric, and asymptotically flat. For an observer located far away from the black hole, equations (33) give the following results:

$$X = -\frac{\xi_{\text{crit}}}{\sin \vartheta_o}, \quad Y = \pm \sqrt{\xi_{\text{crit}} + a^2 \cos^2 \vartheta_o - \xi_{\text{crit}}^2 \cot^2 \vartheta_o}. \quad (34)$$

The  $X$  and  $Y$  contours define the shadow boundary for rotating black hole with scalar hair in beyond Horndeski theory. We present the shadow boundary for a range of parameter samples in Figs. 8, 9 and 10. As we can see, for  $Q < 0$  the shadow of a rotating black hole with scalar hair in beyond Horndeski theory exhibits a larger area compared to that of the Kerr black hole. Conversely, for  $Q > 0$  the area of the shadow is smaller than that of the Kerr black hole. As we observe in Fig. 8, for  $Q > 0$ , increasing the scalar hair parameter  $Q$  results in a reduction in the size of the black hole's shadow, while simultaneously increasing its oblateness. Conversely, from Fig. 9 we deduce that for  $Q < 0$  a decrease in  $Q$  leads to an enlargement of the shadow's size, accompanied by a reduction in its oblateness. Finally, Fig. 10 investigates the impact of the spin parameter  $a$ , demonstrating that for a fixed value of  $Q$  an increase in  $a$  causes a greater distortion of the shadow, with the shadow size diminishing accordingly. These observations reveal the intricate interplay between the scalar hair parameter  $Q$  and the spin parameter  $a$  in shaping the rotating black hole with scalar hair in beyond Horndeski gravity's shadow characteristics.

The EHT collaboration, utilizing VLBI technology, captured the event horizon-scale image of the supermassive black hole M87\* [65, 66]. This significant observation offers a unique opportunity to probe gravity in the strong-field

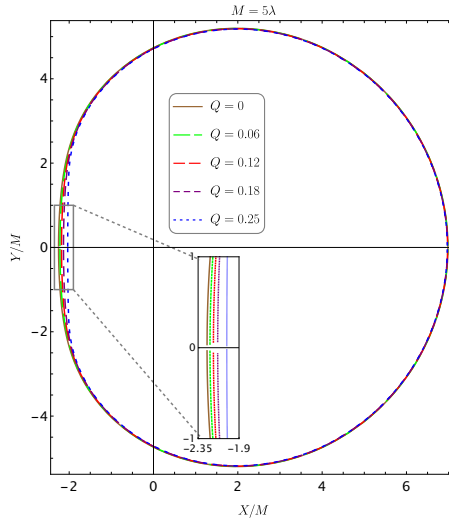


FIG. 8: The boundary of rotating black hole with scalar hair in beyond Horndeski gravity shadow, with varying parameter  $Q > 0$ , setting  $a = 0.99$  and  $\vartheta_o = \frac{\pi}{2}$ .

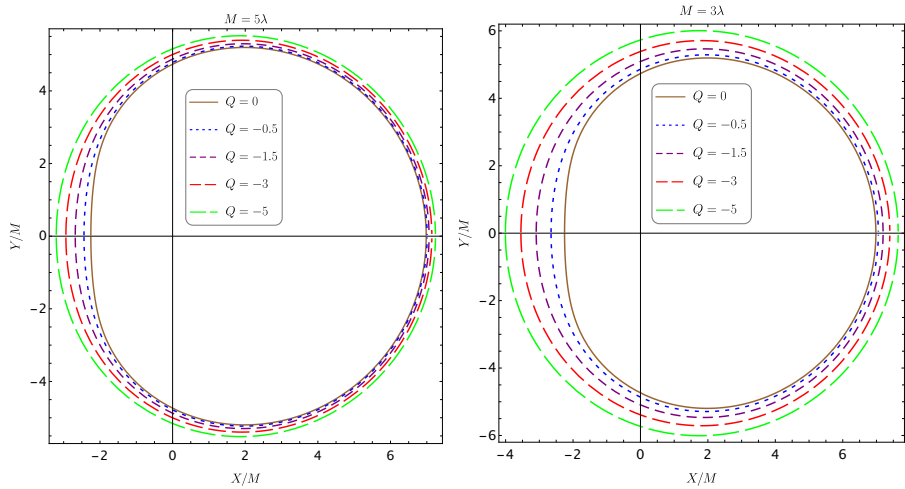


FIG. 9: The boundary of rotating black hole with scalar hair in beyond Horndeski gravity shadow, with varying parameter  $Q < 0$ , setting  $a = 0.99$  and  $\vartheta_o = \frac{\pi}{2}$ .

regime and refines our understanding of black holes. The M87\* shadow appears nearly circular with a crescent shape, exhibiting a circularity deviation of  $\Delta C \leq 0.10$  (10%), measured as the root-mean-square deviation from the average shadow radius. The angular size of the emission region,  $\theta_d$ , in the observed image is  $42 \pm 3$   $\mu$ as [65, 66], and the observed image is consistent with the modeled shadow of a Kerr black hole [65, 66], which can further be used to place constraints on modified gravity models.

The boundary of a black hole shadow is described by polar coordinates  $(R(\varphi), \varphi)$ , with the origin at the shadow's center  $(X_c, Y_c)$ , where  $X_c = (X_r - X_l)/2$  and  $Y_c = 0$ . The average shadow radius,  $\bar{R}$ , is defined as [102].

$$\bar{R}^2 = \frac{1}{2\pi} \int_0^{2\pi} R^2(\varphi) d\varphi, \quad (35)$$

where

$$R(\varphi) = \sqrt{(X - X_c)^2 + (Y - Y_c)^2} \text{ and } \varphi \equiv \tan^{-1} \left( \frac{Y - Y_c}{X - X_c} \right).$$

In this context,  $\varphi$  denotes the angle formed between the  $x$ -axis and the vector that links the center  $(X_c, Y_c)$  to a point  $(X, Y)$  located on the edge of the shadow. Moreover, the circularity deviation  $\Delta C$ , i.e. the deviation from a perfect

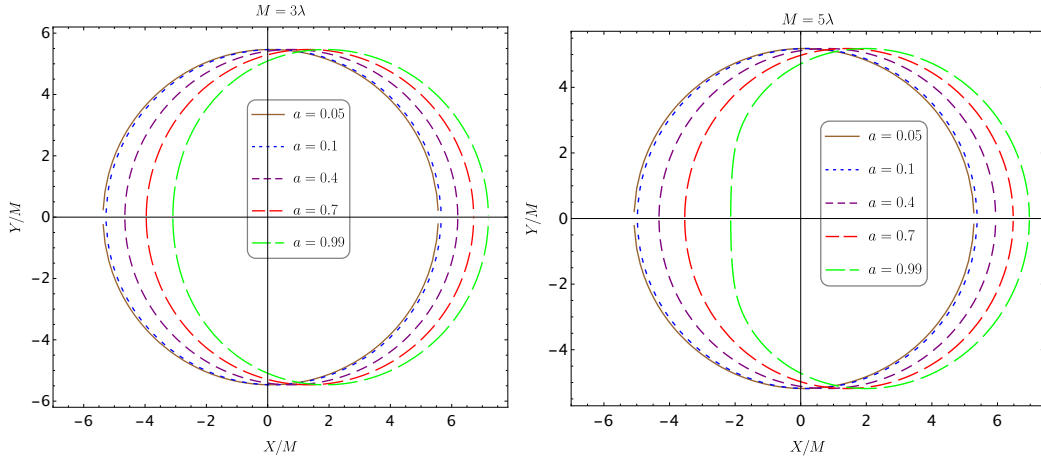


FIG. 10: The boundary of rotating black hole with scalar hair in beyond Horndeski gravity shadow, with varying parameter  $a$ , setting  $Q = -1.5$  and  $\vartheta_o = \frac{\pi}{2}$ .

circular shape, is quantified by [102]

$$\Delta C = \frac{1}{\bar{R}} \sqrt{\frac{1}{2\pi} \int_0^{2\pi} (R(\varphi) - \bar{R})^2 d\varphi}. \quad (36)$$

This measure will be valuable for comparing theoretical predictions of rotating black hole with scalar hair in beyond Horndeski gravity shadows with the observations made by the Event Horizon Telescope (EHT) [102]. Finally, the angular diameter of the shadow, denoted as  $\theta_d$ , is given by [97]

$$\theta_d = \frac{R_{sh}}{d}, \quad R_{sh} = \sqrt{\frac{2}{\pi} \int_{r_p^{min}}^{r_p^{max}} \left( Y(r_p) \frac{dX(r_p)}{dr_p} \right) dr_p}. \quad (37)$$

By modeling M87\* as a rotating black hole with primary scalar hair in beyond Horndeski theory, we can compute the circularity deviation  $\Delta C$  based on the metric given in (8), and then use the results from the EHT observations to impose constraints on the model parameters. The EHT observations indicated that  $\Delta C \leq 0.1$ . To more accurately reference the EHT observations, we will assume  $\vartheta_o = \vartheta_{jet} = 17^\circ$  for M87\*, as the jet inclination relative to the line-of-sight for M87\* is estimated to be  $17^\circ$  [103].

A reliable estimate of the mass of M87\* is essential for translating shadow observables into constraints on the underlying spacetime parameters. Although independent mass determinations do not yet fully coincide [104], we adopt for the present analysis the EHT value  $M \simeq 6.5 \times 10^9 M_\odot$  [65, 66], together with a source distance  $d = 16.8$  Mpc. In Fig. 11 we present the circularity deviation  $\Delta C$  for an observer inclination angle  $\vartheta_o = 17^\circ$ . We find that the condition  $\Delta C \leq 0.10$  is satisfied throughout the explored  $(a, Q)$  parameter space, indicating that the current circularity constraint does not exclude rotating black holes with primary scalar hair in beyond-Horndeski gravity for this viewing configuration.

We now proceed to calculate the angular diameter of the shadow, which, in addition to the parameters  $a$ ,  $Q$ , and  $\vartheta_o$ , also depends on the black hole mass  $M$  and the distance  $d$ . In Fig. 12 we show the angular diameter as a function of  $a$  and  $Q$ . The green curves represent the 39  $\mu$ as bound from EHT, as well as the  $1\sigma$  uncertainty bound for the angular diameter  $\theta_d$  of M87\*, with the enclosed region representing the parameter space  $(Q, a)$  that aligns with the M87\* observations.

The circular asymmetry in the M87\* shadow can be expressed in terms of the axial ratio  $D_x$ , which is defined as the ratio of the major to the minor diameter of the shadow [65, 66]. The axis ratio is given by [105]

$$D_x = \frac{\Delta Y}{\Delta X}. \quad (38)$$

The axial ratio  $D_x$  is expected to lie within the range  $1 < D_x \lesssim 4/3$ , in agreement with the EHT observations of M87\* [65, 66]. In fact,  $D_x$  provides an alternative way to quantify the circularity deviation  $\Delta C$ . The EHT observations reveal that the reconstructed emission ring of M87\* closely approximates a circle, with an axial ratio of 4:3, which

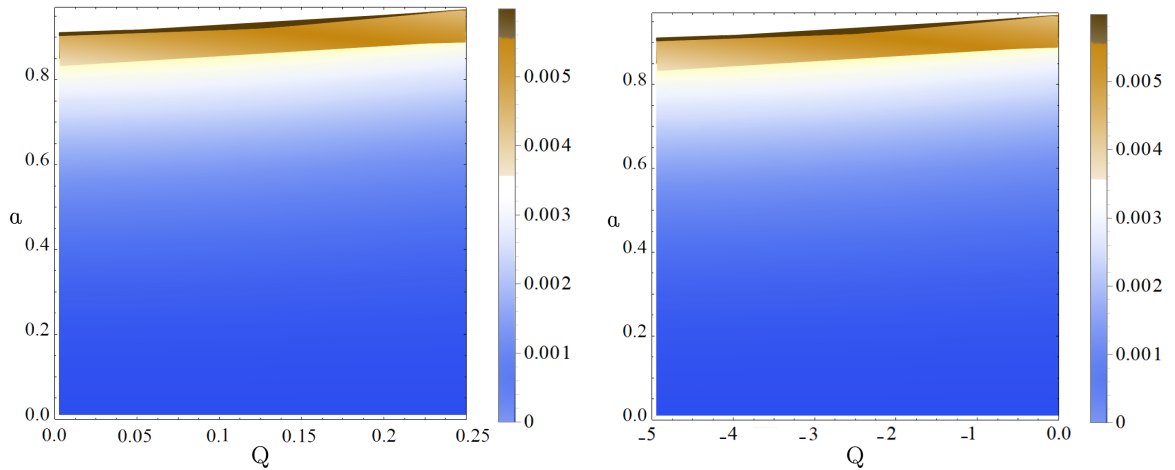


FIG. 11: The circularity deviation  $\Delta C$  for rotating black hole with scalar hair in beyond Horndeski theory shadow, as a function of the parameters  $a$  and  $Q$ , is in agreement with the EHT observations of the M87\* black hole, where  $\Delta C \leq 0.1$  is satisfied across the entire parameter space of  $a$  and  $Q$ . The parameters for M87\* used in this analysis are  $M = 6.5 \times 10^9 M_\odot$  and  $d = 16.8$  Mpc, and the inclination angle considered is  $\vartheta_o = 17^\circ$ . The white region represents the forbidden parameter space.

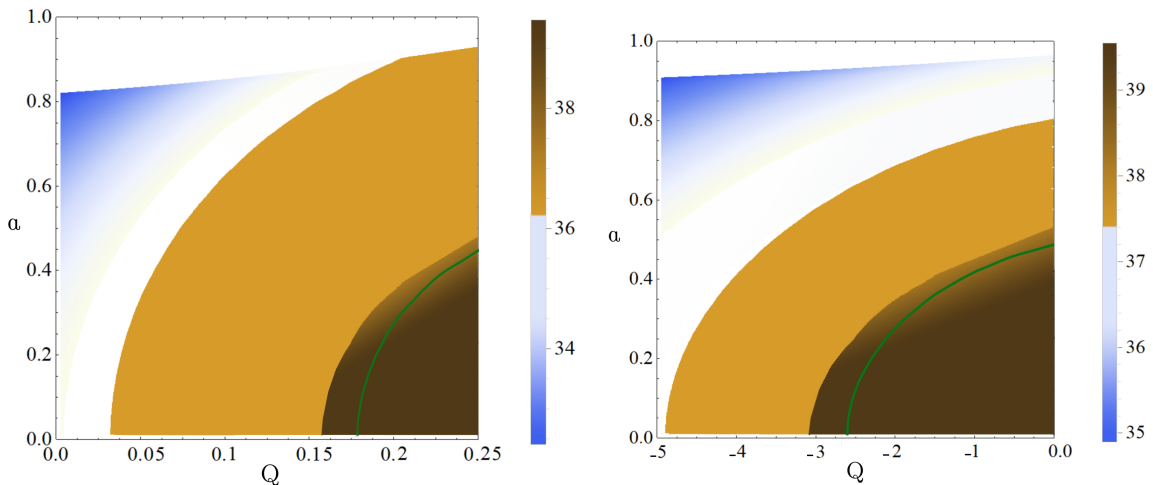


FIG. 12: The angular diameter  $\theta_d$  of the rotating black hole with scalar hair in beyond Horndeski theory shadow as a function of the parameters  $a$  and  $Q$ . The green solid curve corresponds to  $\theta_d = 39 \mu\text{as}$ , which lies within the  $1\sigma$  region of the measured angular diameter  $\theta_d = 42 \pm 3 \mu\text{as}$  for the M87\* black hole, as reported by the EHT. The parameters for M87\* used in this analysis are  $M = 6.5 \times 10^9 M_\odot$  and  $d = 16.8$  Mpc, and the inclination angle considered is  $\vartheta_o = 17^\circ$ . The white region represents the forbidden parameter space.

corresponds to  $\Delta C \leq 0.1$  [65, 66]. The axial ratio is presented as a density plot in Fig. 13, where it is clear that  $1 < D_x \lesssim 4/3$  holds across the entire parameter space  $(Q, a)$ . This result is in remarkable agreement with the EHT images of M87\*, suggesting that the observational data from M87\* does not rule out rotating black holes with scalar hair in beyond Horndeski theory.

#### IV. PHENOMENOLOGICAL IMPLICATIONS AND PARAMETER SENSITIVITY

Having established the null geodesic structure and the corresponding shadow construction, we now examine the observational implications of the rotating primary scalar-hair solutions. The shadow boundary provides a direct mapping between unstable photon orbits and measurable quantities on the observer's sky, and therefore constitutes

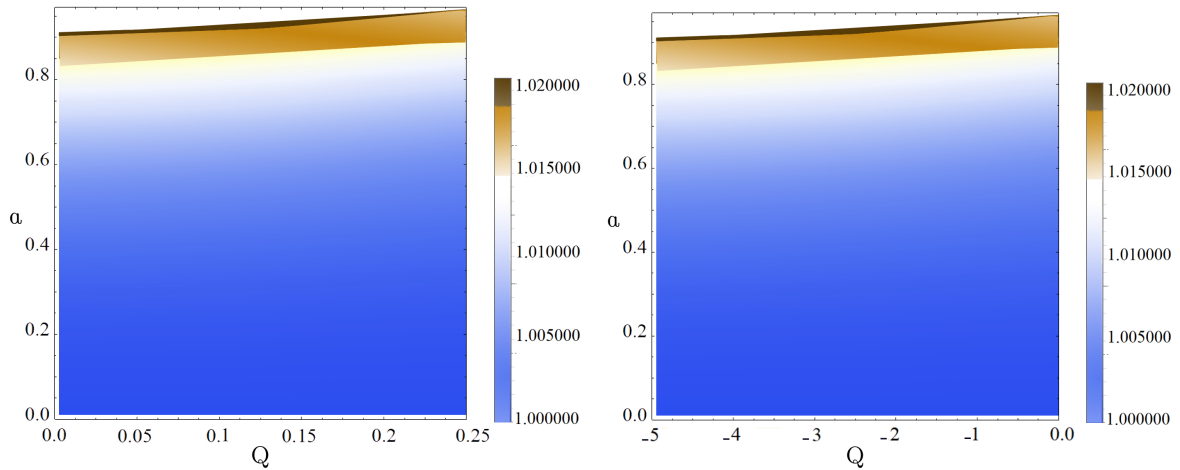


FIG. 13: The axis ratio observable  $D_x$  for rotating black hole with scalar hair in beyond Horndeski theory shadow as a function of the parameters  $a$  and  $Q$ , at an inclination angle  $\vartheta_o = 17^\circ$ . In accordance with the EHT results for M87\*, the condition  $1 < D_x \lesssim 4/3$  is satisfied across the entire parameter space. The white region represents the forbidden region.

a sensitive probe of deviations from the Kerr geometry. In the present model the spacetime is characterized by four parameters: the mass  $M$ , spin  $a$ , scalar hair parameter  $Q$ , and observer inclination angle  $\vartheta_o$ . While  $M$  sets the overall angular scale of the shadow, the parameters  $(a, Q)$  control its morphology. The spin primarily introduces asymmetry and displacement, whereas the scalar hair modifies the effective radial potential of photon motion, thereby altering the size and distortion of the photon region. This distinction allows, in principle, for observational separation between rotation-induced and hair-induced effects, although partial degeneracies may arise.

In what follows, we quantify the sensitivity of the shadow observables to variations in  $(a, Q)$  and assess their compatibility with current Event Horizon Telescope measurements. We focus in particular on the angular diameter  $\theta_d$ , the circularity deviation  $\Delta C$ , and the axis ratio  $D_x$ , which provide complementary measures of shadow size and distortion and thus offer a direct interface between theory and horizon-scale imaging data.

### A. Impact of scalar hair on shadow morphology

The presence of primary scalar hair leads to characteristic modifications of the black hole shadow, reflecting the altered structure of null geodesics in the strong-field regime. As demonstrated in the previous section, these effects manifest in both the overall scale of the shadow and its geometric deformation, providing a phenomenological imprint of beyond Horndeski gravity on horizon-scale observables.

A salient feature of the shadow morphology is the distinct role played by the scalar hair parameter  $Q$  compared to the spin parameter  $a$ . While rotation primarily introduces asymmetry and horizontal displacement of the shadow, scalar hair predominantly affects its size and degree of circularity. In particular, negative values of  $Q$  systematically increase the shadow radius while suppressing shape distortions, whereas positive values of  $Q$  lead to a reduced shadow size accompanied by enhanced deformation. This behavior is evident across a wide range of spin parameters and persists for observationally relevant inclination angles.

The circularity deviation  $\Delta C$ , shown in Fig. 11, remains below the observational bound reported by the Event Horizon Telescope throughout the explored parameter space. This indicates that the inclusion of primary scalar hair does not necessarily produce strongly noncircular shadows, even for moderately large deviations from the Kerr geometry. From a phenomenological perspective, this result implies that near-circular shadow shapes do not uniquely favor Kerr black holes and may also arise in scalar-tensor extensions of general relativity.

In contrast, the angular diameter of the shadow exhibits a stronger sensitivity to the scalar hair parameter, as illustrated in Fig. 12. Variations in  $Q$  induce measurable changes in the effective photon sphere radius, leading to systematic shifts in the predicted angular size of the shadow. These deviations originate from genuine modifications of the radial null effective potential and therefore reflect intrinsic geometric departures from Kerr, rather than coordinate artifacts. Nevertheless, for the case of M87\*, the predicted angular diameters remain within current observational uncertainties, underscoring the limited resolving power of present data.

Taken together, these results demonstrate that scalar hair leaves a subtle but coherent imprint on shadow mor-

phology. The combined behavior of shadow size and shape indicates that scalar-tensor corrections primarily rescale the photon region while preserving near-circularity for a broad range of parameters. This phenomenological pattern distinguishes the effects of scalar hair from those induced solely by rotation and motivates the use of multiple shadow observables in future tests of gravity.

### B. Degeneracies with spin and observational outlook

A central challenge in interpreting black hole shadow observations is the presence of degeneracies among the parameters that govern the spacetime geometry. In the rotating scalar-hairy black hole considered here, both the spin parameter  $a$  and the scalar hair parameter  $Q$  influence the shadow size and shape, leading to overlapping phenomenological signatures that complicate parameter inference.

As illustrated by the distortion parameter and axis-ratio behavior in Fig. 13, different combinations of  $a$  and  $Q$  can produce shadows with comparable degrees of deformation. In particular, an increase in positive scalar hair can mimic the effect of higher spin by reducing the shadow size and enhancing asymmetry, whereas negative scalar hair counteracts spin-induced distortions by enlarging and circularizing the shadow. This interplay gives rise to a partial degeneracy in shadow observables, whereby distinct regions of the  $(a, Q)$  parameter space yield nearly indistinguishable shadow morphologies.

This degeneracy is further reflected in the behavior of the circularity deviation and angular diameter shown in Figs. 11 and 12. While the circularity deviation remains below the current EHT bound across the allowed parameter space, its weak sensitivity limits its ability to disentangle scalar hair from rotational effects. The angular diameter provides stronger discriminatory power, as it responds more directly to modifications of the effective photon sphere radius. However, even this observable is subject to degeneracies when uncertainties in the black hole mass, distance, and inclination angle are taken into account.

From an observational standpoint, these results indicate that shadow morphology alone is insufficient to uniquely constrain the scalar hair parameter at the current level of experimental precision. The degeneracy between  $a$  and  $Q$  implies that constraints derived from a single observable may be systematically biased if Kerr geometry is assumed *a priori*. A robust test of scalar-tensor gravity therefore requires a multi-observable approach that combines shadow size, shape, and displacement with independent astrophysical information.

Looking ahead, future horizon-scale imaging experiments are expected to significantly improve the situation. The next-generation Event Horizon Telescope, with enhanced baseline coverage and sensitivity, may reduce uncertainties in the shadow diameter and shape to a level where subtle deviations induced by scalar hair become detectable. In parallel, incorporating complementary probes, such as polarization measurements, time-dependent imaging, or constraints from accretion-flow dynamics, may help break the degeneracy between spin and scalar hair.

In summary, while current EHT observations do not exclude rotating black holes with primary scalar hair in beyond-Horndeski gravity, the degeneracies identified here define clear phenomenological targets for future observations. Improved imaging precision and multi-channel analyses will be essential for distinguishing scalar-hairy black holes from their Kerr counterparts and for testing gravity in the strong-field regime.

## V. CONCLUDING REMARKS

In this work we have investigated the horizon-scale phenomenology of rotating black holes endowed with genuine primary scalar hair in beyond Horndeski gravity. Starting from the static solution we generated a rotating configuration via a revised Newman-Janis procedure and analyzed its horizon structure, ergoregion properties, and null geodesic dynamics. The resulting spacetime is characterized by an independent scalar hair parameter  $Q$ , in addition to the mass  $M$  and spin  $a$ , providing a well-defined departure from the Kerr geometry that preserves asymptotic flatness and regularity.

A central goal of this work was to determine how this primary scalar hair modifies the photon region and the observable black hole shadow. By solving the Hamilton-Jacobi equations and deriving the critical impact parameters analytically, we constructed the full photon region and shadow boundary for arbitrary  $(a, Q, \vartheta_0)$ . We showed that scalar hair induces systematic and sign-dependent modifications of the shadow morphology. In particular, negative scalar hair ( $Q < 0$ ) enlarges the shadow and reduces its oblateness, whereas positive scalar hair ( $Q > 0$ ) shrinks the shadow and enhances its distortion. These effects originate from genuine modifications of the radial potential governing null geodesics and therefore reflect intrinsic changes in the spacetime geometry rather than coordinate artifacts.

An important result of our analysis is the distinct phenomenological role played by scalar hair compared to rotation. While the spin parameter  $a$  primarily controls asymmetry and displacement of the shadow, the scalar hair parameter

$Q$  predominantly rescales the photon region and alters the effective photon-sphere structure. This difference leads to a characteristic interplay between  $(a, Q)$ , generating partial degeneracies in shadow observables. In particular, certain combinations of positive scalar hair and higher spin can mimic Kerr-like distortions, while negative scalar hair can counteract spin-induced asymmetries. A central novelty of the present analysis is the explicit identification and quantification of this degeneracy between rotation and primary scalar hair.

Modeling M87\* as a rotating black hole with primary scalar hair, we confronted the theory with the current EHT constraints on the circularity deviation, angular diameter, and axis ratio. We found that the circularity bound  $\Delta C \leq 0.1$  and the axis ratio constraint  $1 < D_x \lesssim 4/3$  are satisfied across the full explored parameter space for  $\vartheta_o = 17^\circ$ . The angular diameter constraint  $\theta_d = 42 \pm 3 \mu\text{as}$ , however, restricts the allowed  $(a, Q)$  region more significantly, especially for  $Q > 0$ . The scalar-hair-induced deviations in  $\theta_d$  are typically of order  $\mathcal{O}(\mu\text{as})$ , placing them close to the current observational sensitivity.

These findings demonstrate that present EHT data do not exclude rotating black holes with primary scalar hair in beyond Horndeski gravity, but they already constrain the parameter space in a nontrivial manner. At the same time, the small magnitude of the deviations highlights the need for improved angular resolution and multi-observable analyses in order to break the degeneracy between scalar hair and rotation. Future facilities such as the next-generation EHT and space-based VLBI missions are expected to significantly reduce uncertainties in shadow diameter and shape, potentially allowing for direct discrimination between Kerr and scalar-hairy configurations.

In summary, black hole shadows provide a powerful probe of strong-field gravity beyond the Kerr paradigm. The rotating primary scalar-hairy solutions studied here offer a theoretically consistent and observationally testable framework within beyond Horndeski gravity. As horizon-scale imaging continues to improve, such models will play an essential role in translating precision observations into constraints on the fundamental degrees of freedom of gravity.

## ACKNOWLEDGMENTS

The Work of K. Nozari and S. Saghafi is supported financially by the INSF of Iran under the grant number 4038520. ENS acknowledges the contribution of the LISA CosWG, and of COST Actions CA18108 “Quantum Gravity Phenomenology in the multi-messenger approach” and CA21136 “Addressing observational tensions in cosmology with systematics and fundamental physics (CosmoVerse)”.

## Appendix A: The revised NJA procedure

Following the procedure introduced in Ref. [78], we consider the following general static line element

$$ds^2 = -G(r)dt^2 + \frac{dr^2}{F(r)} + H(r)(d\theta^2 + \sin^2\theta d\phi^2). \quad (\text{A1})$$

We apply the advanced null coordinates  $(u, r, \theta, \phi)$  defined by

$$dt = dr\sqrt{\frac{1}{F(r)G(r)}} + du, \quad (\text{A2})$$

to find the following nonzero components of the resulting inverse metric tensor

$$g^{\mu\nu} = -(l^\mu n^\nu + l^\nu n^\mu - m^\nu \bar{m}^\mu - m^\mu \bar{m}^\nu), \quad (\text{A3})$$

where we have introduced

$$g^{\mu\nu} = -(l^\mu n^\nu + l^\nu n^\mu - m^\nu \bar{m}^\mu - m^\mu \bar{m}^\nu), \quad (\text{A4})$$

in which

$$\begin{aligned} l^\mu &= \delta_r^\mu, \\ n^\mu &= \sqrt{\frac{F(r)}{G(r)}}\delta_u^\mu - \frac{F(r)}{2}\delta_r^\mu, \\ m^\mu &= \frac{1}{\sqrt{2H(r)}}\left(\delta_\theta^\mu + \frac{i}{\sin\theta}\delta_\phi^\mu\right), \\ \bar{m}^\mu &= \frac{1}{\sqrt{2H(r)}}\left(\delta_\theta^\mu - \frac{i}{\sin\theta}\delta_\phi^\mu\right), \end{aligned} \quad (\text{A5})$$

and  $l_\mu l^\mu = m_\mu m^\mu = n_\mu n^\mu = l_\mu m^\mu = n_\mu m^\mu = 0$  and  $l_\mu n^\mu = -m_\mu \bar{m}^\mu = 1$ .

Next, we proceed to apply the following complex transformation

$$r \rightarrow r + ia \cos \theta, \quad u \rightarrow u - ia \cos \theta, \quad (\text{A6})$$

to the metric tensor by which  $\delta_\nu^\mu$  transform as vectors so that

$$\begin{aligned} \delta_r^\mu &\rightarrow \delta_r^\mu, \\ \delta_u^\mu &\rightarrow \delta_u^\mu, \\ \delta_\theta^\mu &\rightarrow \delta_\theta^\mu + ia \sin \theta (\delta_u^\mu - \delta_r^\mu), \\ \delta_\phi^\mu &\rightarrow \delta_\phi^\mu. \end{aligned} \quad (\text{A7})$$

Moreover, we consider that

$$(G(r), F(r), H(r)) \rightarrow (A(r, \theta, a), B(r, \theta, a), \Psi(r, \theta, a)), \quad (\text{A8})$$

where  $(A(r, \theta, a), B(r, \theta, a), \Psi(r, \theta, a))$  are unknown three-variable real functions. Finally, in order to recover the line element (A1) in the limit  $a \rightarrow 0$ , we assume that

$$\begin{aligned} \lim_{a \rightarrow 0} A(r, \theta, a) &= G(r), \\ \lim_{a \rightarrow 0} B(r, \theta, a) &= F(r), \\ \lim_{a \rightarrow 0} \Psi(r, \theta, a) &= H(r), \end{aligned} \quad (\text{A9})$$

We diverge from the usual NJA approach, which determines the expressions for  $(A(r, \theta, a), B(r, \theta, a), \Psi(r, \theta, a))$  by complexifying the radial coordinate  $r$ . Instead, in our method, we will establish  $(A(r, \theta, a), B(r, \theta, a), \Psi(r, \theta, a))$  based on different criteria and physical arguments. Therefore, the complex transformation (A6) will lead to the following expressions

$$\begin{aligned} l^\mu &= \delta_r^\mu, \\ n^\mu &= \delta_u^\mu \sqrt{\frac{B(r, \theta, a)}{A(r, \theta, a)}} - \frac{1}{2} \delta_r^\mu B(r, \theta, a), \\ m^\mu &= \frac{1}{\sqrt{2\Psi(r, \theta, a)}} \left( \delta_\theta^\mu + ia \sin \theta (\delta_u^\mu - \delta_r^\mu) + \frac{i\delta_\phi^\mu}{\sin \theta} \right), \\ \bar{m}^\mu &= \frac{1}{\sqrt{2\Psi(r, \theta, a)}} \left( \delta_\theta^\mu - ia \sin \theta (\delta_u^\mu - \delta_r^\mu) - \frac{i\delta_\phi^\mu}{\sin \theta} \right). \end{aligned} \quad (\text{A10})$$

Hence, we can find the non-zero components of the transformed inverse metric tensor as follows

$$\begin{aligned} g^{uu} &= \frac{a^2 \sin^2(\theta)}{\Psi(r, \theta, a)}, & g^{u\phi} &= \frac{a}{\Psi(r, \theta, a)}, & g^{r\phi} &= -\frac{a}{\Psi(r, \theta, a)}, \\ g^{rr} &= \frac{a^2 \sin^2(\theta)}{\Psi(r, \theta, a)} + B(r, \theta, a), \\ g^{\theta\theta} &= \frac{1}{\Psi(r, \theta, a)}, & g^{\phi\phi} &= \frac{1}{\sin^2(\theta)\Psi(r, \theta, a)}, \\ g^{ur} &= -\left( \frac{a^2 \sin^2 \theta}{\Psi(r, \theta, a)} + \sqrt{\frac{B(r, \theta, a)}{A(r, \theta, a)}} \right), \end{aligned} \quad (\text{A11})$$

and consequently, the rotating line element in EFCs takes the form

$$\begin{aligned} ds^2 &= du^2(-A(r, \theta, a)) - 2\frac{\sqrt{A(r, \theta, a)}}{\sqrt{B(r, \theta, a)}} dr du - 2a \sin^2 \theta \left( \frac{\sqrt{A(r, \theta, a)}}{\sqrt{B(r, \theta, a)}} - A(r, \theta, a) \right) du d\phi \\ &\quad + \frac{2a \sin^2 \theta \sqrt{A(r, \theta, a)}}{\sqrt{B(r, \theta, a)}} dr d\phi + \Psi(r, \theta, a) d\theta^2 \\ &\quad + \sin^2 \theta \left( a^2 \sin^2 \theta \left( \frac{2\sqrt{A(r, \theta, a)}}{\sqrt{B(r, \theta, a)}} - A(r, \theta, a) \right) + \Psi(r, \theta, a) \right) d\phi^2. \end{aligned} \quad (\text{A12})$$

The crucial step is to transform the line element (A12) into BLCs through a global coordinate transformation, typically represented in the following form

$$du = dt + \lambda(r)dr, \quad d\phi = d\varphi + \chi(r)dr. \quad (\text{A13})$$

In order to ensure the integrability of Eq. (A13), the functions  $\lambda(r)$  and  $\chi(r)$  must depend solely on  $r$ .

The usual NJA typically fails to transform the line element (A12) into BLCs. This is because, in the NJA,  $(A(r, \theta, a), B(r, \theta, a), \Psi(r, \theta, a))$  are determined by the complexification of  $r$ , leaving no free functions to facilitate the transformation into BLCs. However, this limitation does not apply to the revised NJA method, as the functions  $(A(r, \theta, a), B(r, \theta, a), \Psi(r, \theta, a))$  remain unknown. Thus, we can successfully achieve the transformation into BLCs. Taking this into account, we proceed with

$$\lambda(r) = -\frac{K(r) + a^2}{a^2 + F(r)H(r)}, \quad \chi(r) = -\frac{a}{a^2 + F(r)H(r)}, \quad (\text{A14})$$

where

$$K(r) = H(r) \sqrt{\frac{F(r)}{G(r)}}. \quad (\text{A15})$$

Thus, one can obtain

$$\begin{aligned} A(r, \theta, a) &= \frac{\Psi(r, \theta, a) (a^2 \cos^2 \theta + F(r)H(r))}{(K(r) + a^2 \cos^2 \theta)^2}, \\ B(r, \theta, a) &= \frac{a^2 \cos^2 \theta + F(r)H(r)}{\Psi(r, \theta, a)}, \end{aligned} \quad (\text{A16})$$

leading to the line element (8).

- [1] B. Carter, *Phys. Rev. Lett.* **26**, 331 (1971).
- [2] W. Israel, *Phys. Rev.* **164**, 1776 (1967).
- [3] S. W. Hawking, *Commun. Math. Phys.* **25**, 152 (1972).
- [4] G. W. Gibbons, *Commun. Math. Phys.* **45**, 191 (1975).
- [5] M. Zajaček, A. Tursunov, A. Eckart, and S. Britzen, *Mon. Not. Roy. Astron. Soc.* **480**, 4408 (2018), arXiv:1808.07327 [astro-ph.GA].
- [6] K. S. Stelle, *Phys. Rev. D* **16**, 953 (1977).
- [7] E. Di Valentino *et al.* (CosmoVerse Network), *Phys. Dark Univ.* **49**, 101965 (2025), arXiv:2504.01669 [astro-ph.CO].
- [8] F. Zwicky, *Helv. Phys. Acta* **6**, 110 (1933).
- [9] M. Sako *et al.* (SDSS), *Publ. Astron. Soc. Pac.* **130**, 064002 (2018), arXiv:1401.3317 [astro-ph.CO].
- [10] J. L. Sievers *et al.* (Atacama Cosmology Telescope), *JCAP* **10**, 060, arXiv:1301.0824 [astro-ph.CO].
- [11] K. S. Dawson *et al.* (BOSS), *Astron. J.* **145**, 10 (2013), arXiv:1208.0022 [astro-ph.CO].
- [12] E. N. Saridakis *et al.* (CANTATA), *Modified Gravity and Cosmology. An Update by the CANTATA Network*, edited by E. N. Saridakis, R. Lazkoz, V. Salzano, P. Vargas Moniz, S. Capozziello, J. Beltrán Jiménez, M. De Laurentis, and G. J. Olmo (Springer, 2021) arXiv:2105.12582 [gr-qc].
- [13] A. A. Starobinsky, *Phys. Lett. B* **91**, 99 (1980).
- [14] S. Nojiri and S. D. Odintsov, *Phys. Lett. B* **631**, 1 (2005), arXiv:hep-th/0508049.
- [15] D. Lovelock, *J. Math. Phys.* **12**, 498 (1971).
- [16] Y.-F. Cai, S. Capozziello, M. De Laurentis, and E. N. Saridakis, *Rept. Prog. Phys.* **79**, 106901 (2016), arXiv:1511.07586 [gr-qc].
- [17] G. Kofinas and E. N. Saridakis, *Phys. Rev. D* **90**, 084044 (2014), arXiv:1404.2249 [gr-qc].
- [18] S. Bahamonde, C. G. Böhmer, and M. Wright, *Phys. Rev. D* **92**, 104042 (2015), arXiv:1508.05120 [gr-qc].
- [19] L. Heisenberg, *Phys. Rept.* **1066**, 1 (2024), arXiv:2309.15958 [gr-qc].
- [20] A. De, T.-H. Loo, and E. N. Saridakis, *JCAP* **03**, 050, arXiv:2308.00652 [gr-qc].
- [21] G. W. Horndeski, *Int. J. Theor. Phys.* **10**, 363 (1974).
- [22] A. De Felice and S. Tsujikawa, *Phys. Rev. D* **84**, 124029 (2011), arXiv:1008.4236 [hep-th].
- [23] C. Deffayet and D. A. Steer, *Class. Quant. Grav.* **30**, 214006 (2013), arXiv:1307.2450 [hep-th].
- [24] A. Cisterna and C. Erices, *Phys. Rev. D* **89**, 084038 (2014), arXiv:1401.4479 [gr-qc].
- [25] T. Kobayashi, Y. Watanabe, and D. Yamauchi, *Phys. Rev. D* **91**, 064013 (2015), arXiv:1411.4130 [gr-qc].

[26] E. Bellini, A. J. Cuesta, R. Jimenez, and L. Verde, *JCAP* **02**, 053, [Erratum: *JCAP* 06, E01 (2016)], arXiv:1509.07816 [astro-ph.CO].

[27] E. Babichev, C. Charmousis, and A. Lehébel, *Class. Quant. Grav.* **33**, 154002 (2016), arXiv:1604.06402 [gr-qc].

[28] R. Kase and S. Tsujikawa, *Int. J. Mod. Phys. D* **28**, 1942005 (2019), arXiv:1809.08735 [gr-qc].

[29] S. Banerjee, Y.-F. Cai, and E. N. Saridakis, *Class. Quant. Grav.* **36**, 135009 (2019), arXiv:1808.01170 [gr-qc].

[30] T. Kobayashi, *Rept. Prog. Phys.* **82**, 086901 (2019), arXiv:1901.07183 [gr-qc].

[31] Á. D. Kovács and H. S. Reall, *Phys. Rev. D* **101**, 124003 (2020), arXiv:2003.08398 [gr-qc].

[32] S. Bahamonde, M. Caruana, K. F. Dialektopoulos, V. Gakis, M. Hohmann, J. Levi Said, E. N. Saridakis, and J. Sultana, *Phys. Rev. D* **104**, 084082 (2021), arXiv:2105.13243 [gr-qc].

[33] H. Lu and Y. Pang, *Phys. Lett. B* **809**, 135717 (2020), arXiv:2003.11552 [gr-qc].

[34] M. Petronikolou, S. Basilakos, and E. N. Saridakis, *Phys. Rev. D* **106**, 124051 (2022), arXiv:2110.01338 [gr-qc].

[35] S. Mandal, T. Parvez, and S. Shankaranarayanan, *Phys. Rev. D* **109**, L041502 (2024), arXiv:2311.07921 [gr-qc].

[36] F. F. Santos, B. Pourhassan, and E. N. Saridakis, *Fortsch. Phys.* **72**, 2300228 (2024), arXiv:2305.05794 [hep-th].

[37] J. Rayimbaev, K. F. Dialektopoulos, F. Sarikulov, and A. Abdujabbarov, *Eur. Phys. J. C* **83**, 572 (2023), arXiv:2307.03019 [gr-qc].

[38] F. F. Santos, B. Pourhassan, E. N. Saridakis, O. Sokoliuk, A. Baransky, and E. O. Kahya, *JHEP* **12**, 217, arXiv:2410.18781 [hep-th].

[39] C.-Y. Chen, A. De Felice, S. Tsujikawa, and T. Sano, *Phys. Rev. D* **113**, 024027 (2026), arXiv:2509.23134 [gr-qc].

[40] H. Hoshimov, S. Orzuev, F. Atamurotov, and A. Abdujabbarov, *Annals Phys.* **482**, 170209 (2025).

[41] F. F. Santos, B. Pourhassan, and E. N. Saridakis, Black Hole Entropy and Complexity Growth in Horndeski Gravity within the AdS/BCFT Framework (2025), arXiv:2509.23430 [hep-th].

[42] S. Mironov, A. Shtennikova, and M. Valencia-Villegas, *Eur. Phys. J. C* **85**, 1378 (2025), arXiv:2509.16850 [hep-th].

[43] D. Totolou, T. Papanikolaou, and E. N. Saridakis, Primordial black hole dark matter from ultra-slow-roll inflation in Horndeski gravity (2025), arXiv:2512.25044 [gr-qc].

[44] J. Gleyzes, D. Langlois, F. Piazza, and F. Vernizzi, *Phys. Rev. Lett.* **114**, 211101 (2015), arXiv:1404.6495 [hep-th].

[45] M. Zumalacárregui and J. García-Bellido, *Phys. Rev. D* **89**, 064046 (2014), arXiv:1308.4685 [gr-qc].

[46] C. Deffayet, G. Esposito-Farese, and D. A. Steer, *Phys. Rev. D* **92**, 084013 (2015), arXiv:1506.01974 [gr-qc].

[47] E. Babichev, K. Koyama, D. Langlois, R. Saito, and J. Sakstein, *Class. Quant. Grav.* **33**, 235014 (2016), arXiv:1606.06627 [gr-qc].

[48] M. Crisostomi, M. Hull, K. Koyama, and G. Tasinato, *JCAP* **03**, 038, arXiv:1601.04658 [hep-th].

[49] J. Sakstein, H. Wilcox, D. Bacon, K. Koyama, and R. C. Nichol, *JCAP* **07**, 019, arXiv:1603.06368 [astro-ph.CO].

[50] J. Sakstein, E. Babichev, K. Koyama, D. Langlois, and R. Saito, *Phys. Rev. D* **95**, 064013 (2017), arXiv:1612.04263 [gr-qc].

[51] J. Ben Achour, D. Langlois, and K. Noui, *Phys. Rev. D* **93**, 124005 (2016), arXiv:1602.08398 [gr-qc].

[52] D. Langlois and K. Noui, *JCAP* **07**, 016, arXiv:1512.06820 [gr-qc].

[53] J. Ben Achour, M. Crisostomi, K. Koyama, D. Langlois, K. Noui, and G. Tasinato, *JHEP* **12**, 100, arXiv:1608.08135 [hep-th].

[54] A. Dima and F. Vernizzi, *Phys. Rev. D* **97**, 101302 (2018), arXiv:1712.04731 [gr-qc].

[55] R. Kolevatov, S. Mironov, N. Sukhov, and V. Volkova, *JCAP* **08**, 038, arXiv:1705.06626 [hep-th].

[56] R. Kase and S. Tsujikawa, *Phys. Rev. D* **97**, 103501 (2018), arXiv:1802.02728 [gr-qc].

[57] M. Zhu, A. Ilyas, Y. Zheng, Y.-F. Cai, and E. N. Saridakis, *JCAP* **11** (11), 045, arXiv:2108.01339 [gr-qc].

[58] A. Bakopoulos, C. Charmousis, P. Kanti, N. Lecoeur, and T. Nakas, *Phys. Rev. D* **109**, 024032 (2024), arXiv:2310.11919 [gr-qc].

[59] M. Rinaldi, *Phys. Rev. D* **86**, 084048 (2012), arXiv:1208.0103 [gr-qc].

[60] A. Anabalon, A. Cisterna, and J. Oliva, *Phys. Rev. D* **89**, 084050 (2014), arXiv:1312.3597 [gr-qc].

[61] M. Minamitsuji, *Phys. Rev. D* **89**, 064017 (2014), arXiv:1312.3759 [gr-qc].

[62] T. P. Sotiriou and S.-Y. Zhou, *Phys. Rev. D* **90**, 124063 (2014), arXiv:1408.1698 [gr-qc].

[63] A. Maselli, H. O. Silva, M. Minamitsuji, and E. Berti, *Phys. Rev. D* **92**, 104049 (2015), arXiv:1508.03044 [gr-qc].

[64] S. Mukherjee and S. Chakraborty, *Phys. Rev. D* **97**, 124007 (2018), arXiv:1712.00562 [gr-qc].

[65] K. Akiyama *et al.* (Event Horizon Telescope), *Astrophys. J. Lett.* **875**, L1 (2019), arXiv:1906.11238 [astro-ph.GA].

[66] K. Akiyama *et al.* (Event Horizon Telescope), *Astrophys. J. Lett.* **875**, L2 (2019), arXiv:1906.11239 [astro-ph.IM].

[67] S. E. Gralla, *Phys. Rev. D* **103**, 024023 (2021), arXiv:2010.08557 [astro-ph.HE].

[68] T. Johannsen, *Phys. Rev. D* **88**, 044002 (2013), arXiv:1501.02809 [gr-qc].

[69] R. A. Konoplya and A. Zhidenko, *JCAP* **12**, 043, arXiv:1606.00517 [gr-qc].

[70] V. Cardoso and P. Pani, *Living Rev. Rel.* **22**, 4 (2019), arXiv:1904.05363 [gr-qc].

[71] H. Falcke, F. Melia, and E. Agol, *Astrophys. J. Lett.* **528**, L13 (2000), arXiv:astro-ph/9912263.

[72] T. Johannsen, *Class. Quant. Grav.* **33**, 113001 (2016), arXiv:1512.03818 [astro-ph.GA].

[73] C. Bambi, *Rev. Mod. Phys.* **89**, 025001 (2017), arXiv:1509.03884 [gr-qc].

[74] C. Goddi *et al.*, *Int. J. Mod. Phys. D* **26**, 1730001 (2016), arXiv:1606.08879 [astro-ph.HE].

[75] M. Khodadi and E. N. Saridakis, *Phys. Dark Univ.* **32**, 100835 (2021), arXiv:2012.05186 [gr-qc].

[76] D. Psaltis *et al.* (Event Horizon Telescope), *Phys. Rev. Lett.* **125**, 141104 (2020), arXiv:2010.01055 [gr-qc].

[77] K. Jusufi, M. Azreg-Aïnou, M. Jamil, and E. N. Saridakis, *Universe* **8**, 102 (2022), arXiv:2110.07258 [gr-qc].

[78] M. Azreg-Aïnou, *Phys. Rev. D* **90**, 064041 (2014), arXiv:1405.2569 [gr-qc].

[79] S. P. Drake and P. Szekeres, *General Relativity and Gravitation* **32**, 445 (2000), arXiv:gr-qc/9807001 [gr-qc].

[80] L. Amarilla and E. F. Eiroa, *Physical Review D* **85**, 064019 (2012), arXiv:1112.6349 [gr-qc].

[81] P. V. P. Cunha and C. A. R. Herdeiro, *General Relativity and Gravitation* **50**, 42 (2018), arXiv:1801.00860 [gr-qc].

[82] R. Kumar, S. G. Ghosh, and A. Wang, *Phys. Rev. D* **101**, 104001 (2020), arXiv:2001.00460 [gr-qc].

[83] M. Azreg-Aïnou, *Eur. Phys. J. C* **74**, 2865 (2014), arXiv:1401.4292 [gr-qc].

[84] E. T. Newman and A. I. Janis, *J. Math. Phys.* **6**, 915 (1965).

[85] D. Hansen and N. Yunes, *Phys. Rev. D* **88**, 104020 (2013), arXiv:1308.6631 [gr-qc].

[86] T. Johannsen and D. Psaltis, *Phys. Rev. D* **83**, 124015 (2011), arXiv:1105.3191 [gr-qc].

[87] K. Jusufi, M. Jamil, H. Chakrabarty, Q. Wu, C. Bambi, and A. Wang, *Phys. Rev. D* **101**, 044035 (2020), arXiv:1911.07520 [gr-qc].

[88] C. Bambi and L. Modesto, *Phys. Lett. B* **721**, 329 (2013), arXiv:1302.6075 [gr-qc].

[89] J. W. Moffat, *Eur. Phys. J. C* **75**, 175 (2015), arXiv:1412.5424 [gr-qc].

[90] S. Chandrasekhar, *The mathematical theory of black holes* (1985).

[91] R. Penrose, *Riv. Nuovo Cim.* **1**, 252 (1969).

[92] B. Carter, *Phys. Rev.* **174**, 1559 (1968).

[93] J. M. Bardeen and J. A. Petterson, *Astrophys. J. Lett.* **195**, L65 (1975).

[94] K. S. Virbhadra and G. F. R. Ellis, *Phys. Rev. D* **62**, 084003 (2000), arXiv:astro-ph/9904193.

[95] V. Bozza, S. Capozziello, G. Iovane, and G. Scarpetta, *Gen. Rel. Grav.* **33**, 1535 (2001), arXiv:gr-qc/0102068.

[96] S. G. Ghosh, R. Kumar, and S. U. Islam, *JCAP* **03**, 056, arXiv:2011.08023 [gr-qc].

[97] R. Kumar and S. G. Ghosh, *JCAP* **07**, 053, arXiv:2003.08927 [gr-qc].

[98] S. U. Islam, R. Kumar, and S. G. Ghosh, *JCAP* **09**, 030, arXiv:2004.01038 [gr-qc].

[99] H. Gott, D. Ayzenberg, N. Yunes, and A. Lohfink, *Class. Quant. Grav.* **36**, 055007 (2019), arXiv:1808.05703 [gr-qc].

[100] P. V. P. Cunha, J. Grover, C. Herdeiro, E. Radu, H. Runarsson, and A. Wittig, *Phys. Rev. D* **94**, 104023 (2016), arXiv:1609.01340 [gr-qc].

[101] K. Hioki and K.-i. Maeda, *Phys. Rev. D* **80**, 024042 (2009), arXiv:0904.3575 [astro-ph.HE].

[102] C. Bambi, K. Freese, S. Vagnozzi, and L. Visinelli, *Phys. Rev. D* **100**, 044057 (2019), arXiv:1904.12983 [gr-qc].

[103] R. Craig Walker, P. E. Hardee, F. B. Davies, C. Ly, and W. Junor, *Astrophys. J.* **855**, 128 (2018), arXiv:1802.06166 [astro-ph.HE].

[104] S. Vagnozzi, C. Bambi, and L. Visinelli, *Class. Quant. Grav.* **37**, 087001 (2020), arXiv:2001.02986 [gr-qc].

[105] I. Banerjee, S. Chakraborty, and S. SenGupta, *Phys. Rev. D* **101**, 041301 (2020), arXiv:1909.09385 [gr-qc].